



1 Improving Fine Mineral Dust Representation from the Surface to the Column
2 in GEOS-Chem 14.4.1

3 Dandan Zhang^{1*}, Randall V. Martin¹, Xuan Liu^{1,2}, Aaron van Donkelaar¹, Christopher R. Oxford¹,
4 Yanshun Li¹, Jun Meng³, Danny M. Leung⁴, Jasper F. Kok⁵, Longlei Li⁶, Haihui Zhu¹, Jay R. Turner¹, Yu
5 Yan¹, Michael Brauer⁷, Yinon Rudich⁸, and Eli Windwer⁸

6 ¹Department of Energy, Environmental and Chemical Engineering, Washington University in St.
7 Louis, St. Louis, Missouri 63130, United States

8 ²Scripps Institution of Oceanography, University of California San Diego, San Diego, California
9 92093, United States

10 ³Department of Civil and Environmental Engineering, Washington State University, Pullman,
11 Washington 99163, United States

12 ⁴Atmospheric Chemistry Observations and Modeling Laboratory, National Science Foundation
13 National Center for Atmospheric Research, Boulder, Colorado 80301, United States

14 ⁵Department of Atmospheric and Oceanic Sciences, University of California Los Angeles, Los
15 Angeles, California 90095, United States

16 ⁶Department of Earth and Atmospheric Sciences, Cornell University, Ithaca, New York 14853,
17 United States

18 ⁷School of Population and Public Health, University of British Columbia, Vancouver, British
19 Columbia V6T 1Z3, Canada

20 ⁸Department of Earth and Planetary Sciences, Weizmann Institute of Science, Rehovot 76100,
21 Israel

22 *Correspondence to:* Dandan Zhang (dandan.z@wustl.edu)

23



24 **Abstract**

25 Accurate representation of mineral dust remains a challenge for global air quality or climate
26 models due to inadequate parametrization of the emission scheme, removal mechanisms, and
27 size distribution. While various studies have constrained aspects of dust emission fluxes and/or
28 dust optical depth, surface dust concentrations still vary by factors of 5-10 among models. In this
29 study, we focus on improving the simulation of fine dust in the GEOS-Chem chemical transport
30 model, leveraging recent mechanistic understanding of dust source and removal, and reconciling
31 the size differences between models and ground-based measurements. Specifically, we conduct
32 sensitivity simulations using GEOS-Chem in its high performance configuration (GCHP) version
33 14.4.1 to investigate the effects of mechanism or parameter updates. The results are evaluated by
34 comparisons versus Deep Blue satellite-based aerosol optical depth (AOD) and AEROSOL RObotic
35 NETwork (AERONET) ground-based AOD for total column abundance, and versus the Surface
36 Particulate Matter Network (SPARTAN) for surface $PM_{2.5}$ dust concentrations. Reconciling modelled
37 geometric diameter versus measured aerodynamic diameter is important for consistent
38 comparison. The two-fold overestimation of surface fine dust in the standard model is alleviated by
39 36% without degradation of total column abundance by implementing a new physics-based dust
40 emission scheme with better spatial distribution. Further reduction by 16% of the overestimation of
41 surface $PM_{2.5}$ dust is achieved through reducing the mass fraction of emitted fine dust based on the
42 brittle fragmentation theory, and explicit tracking of three additional fine mineral dust size bins with
43 updated parametrization for below-cloud scavenging. Overall, these developments reduce the
44 normalized mean difference against surface fine dust measurements from SPARTAN from 73% to
45 21%, while retaining comparable skill of total column abundance against satellite and ground-
46 based AOD.

47 **1 Introduction**

48 Mineral dust exerts significant impacts on air quality as the most abundant aerosol component by
49 mass globally (Kok et al., 2021), on ecosystem health through nutrient transport and deposition
50 such as phosphorous (Bayon et al., 2024; Swap et al., 1992) and iron (Jickells et al., 2005), and on
51 climate through its direct scattering and absorbing of radiation and indirect modifications of cloud
52 properties (Kok et al., 2017; Liao and Seinfeld, 1998; Mahowald et al., 2014). Despite its
53 importance, accurate representation of mineral dust remains a challenge for global air quality or



54 climate models due to inadequate parametrization of the emission scheme (Darmenova et al.,
 55 2009; Kok, 2011; Leung et al., 2023), removal mechanisms (Jones et al., 2022; Petroff and Zhang,
 56 2010; Ryu and Min, 2022; Wang et al., 2014b; Zhang and Shao, 2014; Zhang et al., 2001), and size
 57 distribution (Kok et al., 2017; Mahowald et al., 2014). Observational constraints from satellite have
 58 been applied to reduce the large uncertainty of simulated mineral dust and its emissions
 59 (Mytilinaios et al., 2023; Ridley et al., 2016). However, intercomparison projects with various
 60 models still suggest large variability within a factor of 2 for the total column abundance of mineral
 61 dust, with even larger variability in surface concentrations and deposition by factors of 5-10
 62 (Huneeus et al., 2011; Uno et al., 2006; Wu et al., 2020).

63 In addition to total column observations, ground-level measurements of mineral dust offer another
 64 promising opportunity to understand mechanisms affecting the accuracy of the surface
 65 concentration simulation and the variable performance from the surface to the total column in
 66 intercomparison projects. The Surface PARTiculate mAtter Network (SPARTAN,
 67 <https://www.spartan-network.org/>, last access: 4 February 2025) is a globally distributed
 68 monitoring network that measures the chemical components of fine particulate matter (PM_{2.5}),
 69 including in arid environments (Liu et al., 2024; Snider et al., 2015). These ground-based
 70 measurements of mineral dust in PM_{2.5} offer new data to evaluate, understand, and improve fine
 71 dust simulation in global models.

72 Dust emissions play a central role in controlling the surface and total column abundance of
 73 mineral dust (Kok et al., 2014; Leung et al., 2023; Tian et al., 2021). The predicted spatial
 74 distribution particularly affects the downwind dust concentrations through long-range transport
 75 and deposition (Prospero, 1999). A new physics-based dust emission scheme (Leung et al., 2023)
 76 includes recent developments in the parametrization of the threshold of friction velocity for dust
 77 mobilization (Martin and Kok, 2018), combined drag partitioning effects due to rocks (Marticorena
 78 and Bergametti, 1995) and vegetation (Pierre et al., 2014a) for a better representation of exerted
 79 surface friction velocity (Leung et al., 2023), and intermittent dust mobilization due to high-
 80 frequency turbulence (Comola et al., 2019). This dust emission scheme has achieved better spatial
 81 correlations of dust column abundance against ground-based and satellite-derived dust optical
 82 depth in the Community Earth System Model version 2 (CESM2) (Leung et al., 2023, 2024).
 83 However, the effects of these new developments of dust emission scheme on the bias against
 84 ground-based measurements of surface fine dust concentrations are less well known and require



85 further investigation.

86 The source and removal of dust in the size bins used in dust parametrizations can vary by orders of
87 magnitude across the broad size range of mineral dust (Kok, 2011; Wang et al., 2014b; Zhang et al.,
88 2001). Accounting for this size heterogeneity among dust bins could enable better representation
89 of the global dust cycle. Prior studies have found an underestimation of coarse dust emissions and
90 an overestimation of fine dust (Kok, 2011; Kok et al., 2017). While various studies have focused on
91 developing the representation of coarse or super coarse dust (Kok et al., 2017; Meng et al., 2022),
92 investigation of the effects of different emission size distributions on ambient fine dust are needed
93 through comparison with in situ fine dust measurements. In addition, the developments and
94 improvements of parallel computing in air quality or climate models (Eastham et al., 2018; Harris et
95 al., 2020; Hu et al., 2018; Martin et al., 2022) offer computational capabilities to extend dust size
96 bins with explicit treatments that could enable better representation of dust, especially over size
97 ranges with rapid variation in processes. While the parametrization of dry deposition has been
98 revisited and evaluated against observations (Emerson et al., 2020), below-cloud or washout
99 scavenging has been generally limited to lumped treatments for fine and coarse aerosols in the
100 bulk models (Jones et al., 2022; Wang et al., 2011, 2014a). Developments of the size-resolved
101 parametrization for below-cloud (washout) scavenging (Wang et al., 2014b) are promising to
102 improve the wet deposition of fine dust, which is especially important in distant downwind regions
103 due to long-range transport.

104 In this study, we implement recent developments of a new dust emission scheme with further
105 refinements including the clay content and wetness in the top soil layer; reducing the dust
106 emissions over wet, snow and vegetation covered land surfaces; while constraining the global and
107 regional source with satellite aerosol optical depth (AOD). We revisit the size distribution of emitted
108 dust, explicitly track mineral dust with geometric diameter less than 2 μm in four size bins, and
109 update the parametrization for size-resolved washout scavenging. We conduct sensitivity
110 simulations using the GEOS-Chem chemical transport model in its high performance configuration
111 (GCHP) to investigate the effects of these developments. We focus on improving the fine dust
112 representation in GCHP for better agreement from the surface to the column, by comparisons
113 against ground-level fine dust measurements, and against the ground-based and satellite-retrieved
114 AOD over dusty regions of the Sahara, the Middle East and Asia.



115 **2 Data sources and model description**

116 **2.1 Data sources**

117 Ground-based AOD measurements are obtained from the Aerosol Robotic Network (AERONET)
 118 Version 3 Level 2 database with improved cloud screening (Giles et al., 2019). We use satellite
 119 retrievals of AOD from the Deep Blue algorithm (Hsu et al., 2019) based on Collection 6.1 of the
 120 Moderate Resolution Imaging Spectroradiometer (MODIS) instrument aboard the satellite
 121 platforms of Terra with local overpass around 10:30 and of Aqua around 13:30, and the Version 2.0
 122 Deep Blue aerosol global product of the Visible Infrared Imaging Radiometer Suite (VIIRS)
 123 instruments aboard the joint NASA/NOAA Suomi National Polar-orbiting Partnership (Suomi NPP)
 124 and NOAA-20 satellites with local overpass around 13:30 (Cao et al., 2014). We choose the Deep
 125 Blue aerosol product due to its optimization for the retrieval of aerosol properties over bright
 126 surfaces, which is typical over arid regions. We average all Deep Blue aerosol products for the year
 127 2018 at a daily basis. Simulated AOD is coincidentally sampled with available daily average Deep
 128 Blue AOD.

129 We use the Version 4.2 Level 3 gridded cloud-free tropospheric aerosol extinction profile product
 130 during daytime and nighttime of the last 15 years (2007–2021) retrieved from the Cloud–Aerosol
 131 Lidar with Orthogonal Polarization (CALIOP) on board the Cloud–Aerosol Lidar Infrared Pathfinder
 132 Satellite Observations (CALIPSO) satellite for climatological aerosol profiles (Young et al., 2018).

133 We use global ground-based data from the Surface Particulate Matter Network (SPARTAN;
 134 <https://www.spartan-network.org/>, last access: 4 February 2025) with filter-based PM_{2.5} chemical
 135 composition data (Liu et al., 2024; Snider et al., 2015). Particles with aerodynamic diameter less
 136 than 2.5 µm are collected on Teflon filters using AirPhoton SS5 sampling stations with a sharp-cut
 137 cyclone (SCC) 1.829 that operates at a target flow rate of 5 liter per minute (Lpm) and analyzed for
 138 fine mineral dust concentrations using X-ray Fluorescence (XRF) and a global mineral dust
 139 equation (Equation (A1); Liu et al., 2022) including correction of attenuation effects due to mass
 140 loading. We use data from sites with at least 10 samples for the 5-year (2019–2023) period after the
 141 network began using XRF. The 5-year averaged surface fine dust concentrations from all 26
 142 SPARTAN sites are listed in Table A1.



143 2.2 GEOS-Chem chemical transport model

144 We use the GEOS-Chem chemical transport model (<https://geoschem.github.io/>, last access: 4
 145 February 2025) in its high-performance configuration (Eastham et al., 2018) version 14.4.1 (The
 146 International GEOS-Chem User Community, 2024)) with improved performance and usability
 147 (Martin et al., 2022). The model is driven by meteorological inputs from GEOS Forward Processing
 148 (GEOS-FP; <https://gmao.gsfc.nasa.gov/>, last access: 4 February 2025) with resolution
 149 $0.25^\circ \times 0.3125^\circ$ (~25 km) and 72 hybrid sigma-pressure vertical levels up to 0.01 hPa.

150 GEOS-Chem simulates detailed oxidant-aerosol chemistry in the troposphere and stratosphere,
 151 with gas-phase mechanism of $\text{HO}_x\text{-NO}_x\text{-BrO}_x\text{-VOC-O}_3$ chemistry (Bey et al., 2001; Wang et al.,
 152 2021), coupled to aerosol chemistry for sulfate-nitrate-ammonium (SNA) aerosol (Park et al.,
 153 2004), black carbon (BC) (Wang et al., 2014a), and primary and secondary organic aerosol (Pai et
 154 al., 2020), sea salt (Jaeglé et al., 2011), and natural and anthropogenic dust (Fairlie et al., 2007;
 155 Meng et al., 2021; Philip et al., 2017; Zhang et al., 2013). The gas-aerosol partitioning for SNA is
 156 computed by the HETP v1.0 thermodynamic module (Miller et al., 2024). We use the simple,
 157 irreversible, direct yield scheme for secondary organic aerosol production (Pai et al., 2020). The
 158 effects of aerosol on photolysis rates are computed with relative humidity dependent aerosol size
 159 distributions and optical properties with improved parametrization for the effective radii of
 160 inorganic and organic aerosols (Latimer and Martin, 2019; Ridley et al., 2012; Zhu et al., 2023) and
 161 updated optical properties for aspherical mineral dust (Singh et al., 2024).

162 The standard dry deposition scheme in GEOS-Chem accounts for gravitational settling,
 163 aerodynamic resistance with respect to turbulent transport within the surface layer, and surface
 164 resistance to particle-surface contact due to Brownian diffusion, impaction, and interception with
 165 an observation constrained parametrization (Emerson et al., 2020; Zhang et al., 2001). The
 166 standard wet deposition scheme includes scavenging in convective updrafts, and in-cloud and
 167 below-cloud scavenging from precipitation (Liu et al., 2001; Wang et al., 2011, 2014a).

168 Emissions for GEOS-Chem are configured using the Harmonized Emissions Component (HEMCO)
 169 module v3.9.1 (Lin et al., 2021). Global anthropogenic emissions are from the Community
 170 Emissions Data System (CEDS) v2 at $0.5^\circ \times 0.5^\circ$ resolution (Feng et al., 2020). Offline emissions of
 171 lightning NO_x (Murray et al., 2012), biogenic VOCs, soil NO_x , sea salt (Weng et al., 2020) and mineral
 172 dust (Sections 2.3 and 4.2) at $0.25^\circ \times 0.3125^\circ$ resolution are included to represent emission



processes at the finest available resolution and to enable consistent emission fluxes across model resolutions. Open fire emissions are from the daily Global Fire Emissions Database (GFED) v4.1s (Giglio et al., 2013) at $0.25^\circ \times 0.25^\circ$ resolution. Other default emission inventories in GCHP v14.4.1 include volcanic SO_2 emissions (Fisher et al., 2011), marine emissions of dimethylsulfide (DMS) (Breider et al., 2017) at $1^\circ \times 1^\circ$ resolution, and ammonia at $0.25^\circ \times 0.25^\circ$ resolution (Bouwman et al., 1997; Croft et al., 2016). We conduct GCHP simulations at C48 (~200 km) resolution for the full year of 2018 following a one-month spin-up.

2.3 Default dust emission scheme

The default dust emission scheme in GEOS-Chem (hereafter GC Dust) originally implemented by Fairlie et al. (2007) is based on the semi-empirical Mineral Dust Entrainment and Deposition (DEAD) emission scheme (Zender et al., 2003) and the GOCART topographical source function (Ginoux et al., 2001) updated to a fine resolution of $0.25^\circ \times 0.25^\circ$ (Meng et al., 2021). The total dust emission flux in $\text{kg m}^{-2} \text{s}^{-1}$ is calculated based on Zender et al. (2003) and Fairlie et al. (2007):

$$F_d = f_{bare} S \varphi Q_s \quad (1)$$

where f_{bare} is the bare ground fraction as specified in Zender et al. (2003) to reduce dust emissions over wet, snow and vegetation covered surfaces:

$$f_{bare} = (1 - A_l - A_{wl})(1 - A_{snow}) \left(1 - \frac{\text{LAI}}{\text{LAI}_{thr}}\right) \quad (2)$$

where A_l , A_{wl} , and A_{snow} is the fraction of land covered by lakes, wetlands, and snow, respectively. LAI is the leaf area index, and LAI_{thr} is the threshold LAI to reduce the bare soil fraction due to vegetation cover, which is set to $0.3 \text{ m}^2 \text{m}^{-2}$ by default.

S is the GOCART topographical source function (Ginoux et al., 2001) updated at fine resolution of $0.25^\circ \times 0.25^\circ$ and multiplied by the fraction of bare surface within each grid cell (Meng et al., 2021); φ is the sandblasting efficiency to convert horizontal saltation flux to vertical dust flux (Marticorena and Bergametti, 1995):

$$\varphi = 10^{13.4 f_{clay} - 4} \quad (3)$$

where f_{clay} is the clay content in the top soil layer and a global constant value of 0.2 is used to



199 reduce excessive sensitivity of dust emission fluxes to f_{clay} (Zender et al., 2003). Q_s is the
 200 horizontal saltation flux as described in Section A2.

201 **2.4 Size distribution of emitted dust**

202 The default size distribution of emitted dust in GEOS-Chem implemented by Zhang et al. (2013) is
 203 based on the Brittle Fragmentation Theory (Kok, 2011) with parameter values optimized using dust
 204 observations from the Interagency Monitoring of Protected Visual Environments (IMPROVE)
 205 ground-based monitoring network in the United States:

$$206 \quad \frac{dV_d}{d \ln D_d} = \frac{D_d}{c_V} \left[1 + \operatorname{erf} \left(\frac{\ln(D_d/\overline{D_s})}{\sqrt{2} \ln \sigma_s} \right) \right] \exp \left[- \left(\frac{D_d}{\lambda} \right)^3 \right] \quad (4)$$

207 where V_d is the normalized volume for emitted dust aerosols in diameter of D_d in μm ; c_V is the
 208 normalization constant to make the integration total of V_d of 1; $\overline{D_s} = 3.4 \mu\text{m}$ is the median diameter
 209 of soil particles; $\sigma_s = 3.0$ is the geometric standard deviation of soil particles; λ is the side crack
 210 propagation length, whose value is $8 \mu\text{m}$ in the default particle size distribution (PSD) used in the
 211 GEOS-Chem (GC PSD), and is $12 \mu\text{m}$ in the Kok PSD (Kok, 2011).

212 Table 1. The binning of mineral dust in 4-bin and 7-bin simulations using GEOS-Chem. The
 213 geometric diameter range is listed in the bracket adjacent to each size bin in unit of μm .

4-bin simulation	7-bin simulation
	DSTbin1 (0.2–0.36)
DST1 (0.2–2.0)	DSTbin2 (0.36–0.6)
	DSTbin3 (0.6–1.2)
	DSTbin4 (1.2–2.0)
DST2 (2.0–3.6)	DSTbin5 (2.0–3.6)
DST3 (3.6–6.0)	DSTbin6 (3.6–6.0)
DST4 (6.0–12.0)	DSTbin7 (6.0–12.0)

214

215 Dust aerosols are conventionally separated into several dust bins to compromise between
 216 accuracy and computational expense (Ginoux et al., 2001; Zender et al., 2003). Table 1
 217 summarizes the binning of mineral dust in 4-bin and 7-bin simulations. In the GEOS-Chem
 218 standard bulk configuration used here, 4 dust size bins are used including DST1 to DST4 covering



geometric diameter of 0.2–12.0 μm (Fairlie et al., 2007). For DST1, 4 sub-bins of 0.2–0.36 μm , 0.36–0.6 μm , 0.6–1.2 μm , and 1.2–2.0 μm are further separated for heterogeneous chemistry and AOD calculations, with shared emission, transport and deposition altogether as DST1 (Fairlie et al., 2007). To improve submicron dust representation, we implement full separation of the 7 dust bins for coupled physical and chemical processes in GEOS-Chem, as discussed in Section 4.3.2.

2.5 Reconciling geometric and aerodynamic diameter

A recent study has emphasized the importance of reconciling the geometric diameter used in models and the aerodynamic diameter used in ground-based measurements, especially for mineral dust with higher particle density of $\sim 2500 \text{ kg m}^{-3}$ than the standard density of 1000 kg m^{-3} and with aspherical shapes observed in the atmosphere (Huang et al., 2021). We harmonize the differences between geometric diameter and aerodynamic diameter based on Reid et al. (2003):

$$D_{aer} = D_{geo} \sqrt{\frac{\rho_d}{\chi \rho_0}} \quad (5)$$

where D_{aer} is the aerodynamic diameter; D_{geo} is the geometric diameter; $\rho_d = 2500 \text{ kg m}^{-3}$ is the dust density; $\rho_0 = 1000 \text{ kg m}^{-3}$ is the standard spherical particle density; χ is the dynamic shape factor calculated by $\chi = \frac{1}{2} \left(F_s^{1/3} + \frac{1}{F_s^{1/3}} \right)$ and F_s is Stokes form factor (Bagheri and Bonadonna, 2016; Huang et al., 2020) which can be calculated by $\text{HWR} \left(\frac{1}{\text{AR}} \right)^{1.3}$ where $\text{AR} = 1.70 \pm 0.03$ is the particle length to width ratio, and $\text{HWR} = 0.40 \pm 0.07$ is the particle height to width ratio (Huang et al., 2021). With this conversion, the aerodynamic diameter of 2.5 μm corresponds to the geometric diameter of 1.7 μm . The mass fraction of each simulated dust size bin to the total fine dust mass concentrations can be calculated by the integration of the dust size distribution of Equation (4) with the λ value of 12 μm of the default PSD used in the GEOS-Chem (GC PSD), which is 68% of DST1 with diameter of 0.2–2.0 μm .

In addition to harmonizing different size types used in models and measurements, prior studies also suggested that the sharpness of size cut-off of different inlets used to collect $\text{PM}_{2.5}$ samples can affect the measured concentrations (Kenny et al., 2000; Peters et al., 2001). To evaluate the effects, we obtain the dust size distributions of different inlets by multiplying their penetration efficiencies (Peters et al., 2001) and GC PSD (Equation (4)).



Figure 1 shows the effects of the sharpness of size cut on the size distribution of collected dust $PM_{2.5}$ samples. All four inlets have a penetration efficiency of near unity for dust with geometric diameter less than $1.0\ \mu m$, which diminishes to 0.5 at a geometric diameter of $1.7\ \mu m$ and further diminishes with increasing diameter. The Well Impactor Ninety-Six (WINS) referenced by the Federal Reference Method (FRM) exhibits the sharpest size cut. The corresponding dust PSD is sharply attenuated for geometric diameters greater than $1.7\ \mu m$. The resultant effects on the mass fractions of the dust size bin to be included in dust $PM_{2.5}$ are small, with the mass fraction of DST1 ranging from 65–70%. The mass fraction based on SCC 1.829 as used by SPARTAN differs by only -0.4% from that based on the original GC PSD without inlet penetration correction. In our Base simulation using the standard version of GEOS-Chem, we calculate surface $PM_{2.5}$ dust as 67.6% of DST1 to account for both aerodynamic diameter and inlet collection efficiency. Neglect of these effects would have increased simulated $PM_{2.5}$ dust concentrations by a factor of 2.

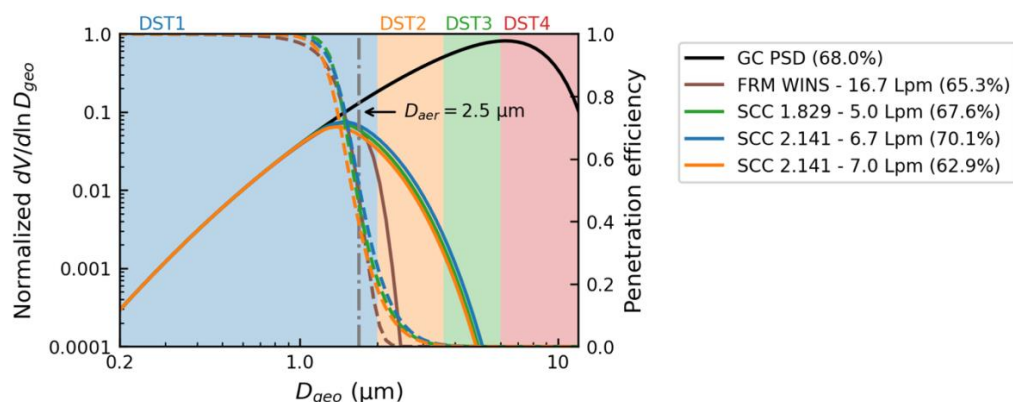


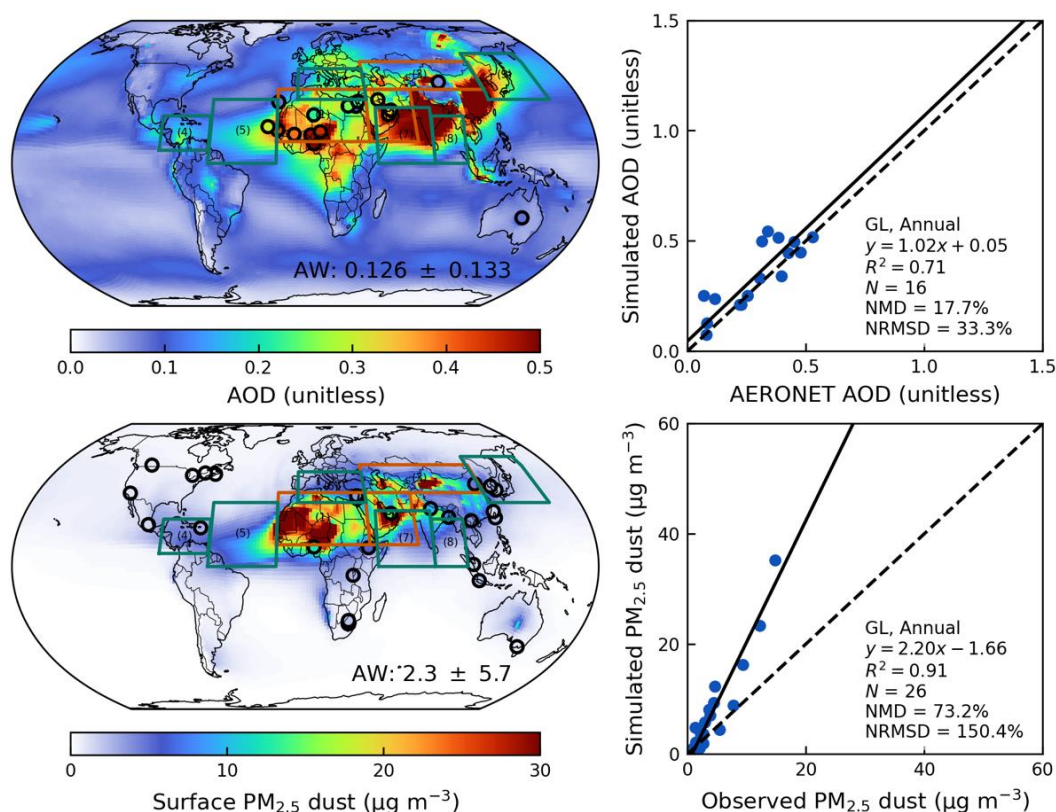
Figure 1. Normalized particle size distribution (PSD) used by default in GEOS-Chem (GC PSD) in solid black with left axis; penetration efficiencies for different types of $PM_{2.5}$ inlets shown in dashed colored lines with right axis, including the Well Impactor Ninety-Six (WINS), and three types of Sharp-Cut Cyclone (SCC) inlets; Solid colored lines show the adjusted GC PSD collected by different inlets. Grey dash-dotted line indicates the corresponding geometric diameter of $1.7\ \mu m$ for the aerodynamic diameter of $2.5\ \mu m$. Filled rectangles indicate size ranges of 4 dust size bins. Percentages adjacent to GC PSD and different inlets are mass fractions of DST1 for the calculation of $PM_{2.5}$ dust concentrations.



267 **3 Strong overestimation of surface fine dust**

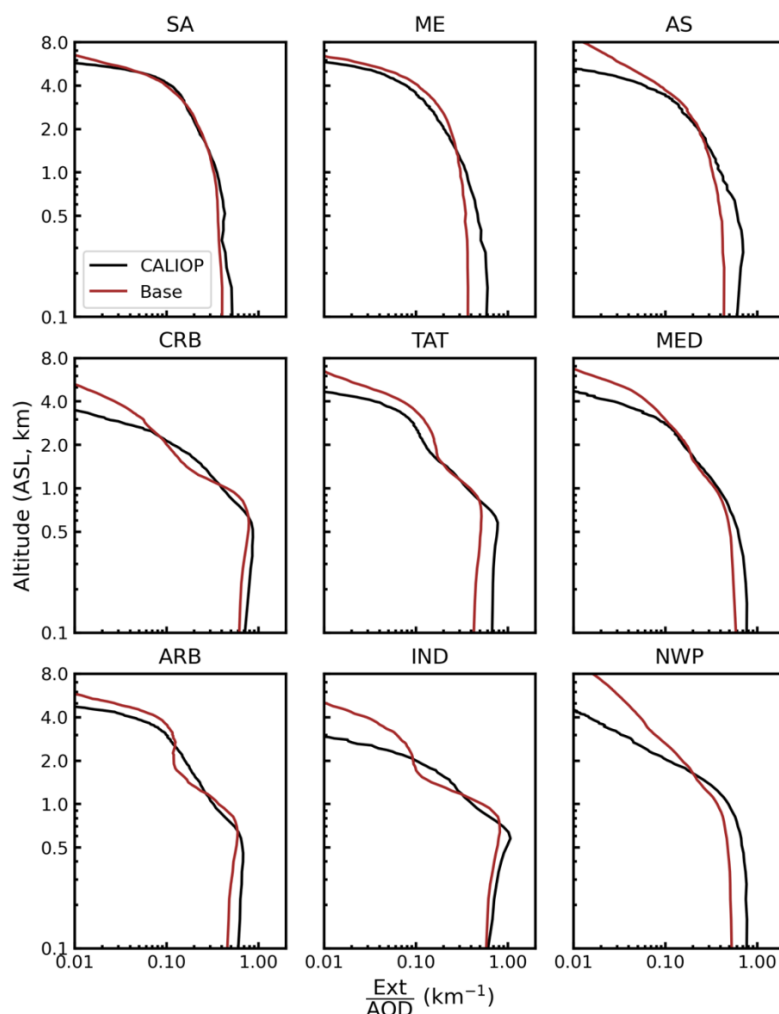
268 Figure 2 shows the spatial distributions of the annual total column AOD and surface PM_{2.5} dust
269 from AERONET, SPARTAN, and the Base simulation using the standard version of GEOS-Chem in
270 the year of 2018. Mineral dust largely determines the AOD in AERONET and GEOS-Chem over and
271 downwind of the main dust source regions including the Sahara, Middle East, and the Taklamakan
272 and Gobi deserts in Asia. The simulated AOD over dusty regions (defined here as $AOD_{Dust}/AOD >$
273 0.5) exhibits a high degree of consistency versus the ground-based observations of AERONET AOD
274 with the regression slope near unity and R^2 of 0.7. However, the simulated surface PM_{2.5} dust
275 exhibits a pronounced overestimation by a factor of 2.2 compared to the ground-based
276 measurements of SPARTAN. Simulated PM_{2.5} dust is overestimated at the dusty sites of Abu Dhabi
277 in the United Arab Emirates by 143%, Ilorin in Nigeria by 100%, and Kanpur in India by 75%.

278 Figure 3 shows the vertical profile of the aerosol extinction normalized by AOD over main dust
279 source regions and associated downwind regions, to understand the significant performance
280 difference between the surface and the column. The simulated vertical profile shows excellent
281 agreement against the 15-year (2007 to 2021) climatological mean extinction vertical profile from
282 the CALIOP, indicating the vertical distribution of mineral dust is not the main driver of the
283 performance discrepancy between the surface and the column.



284

285 Figure 2. Annual simulated aerosol optical depth (AOD) and comparison against ground-based
 286 observations from AERONET over dusty regions ($AOD_{Dust}/AOD > 0.5$) (top); Annual simulated
 287 surface $PM_{2.5}$ dust and comparison against ground-based measurements from SPARTAN (bottom)
 288 from the Base simulation in the year of 2018. Filled circles on the maps represent ground-based
 289 observations from SPARTAN and AERONET. Inset values at the bottom right of the maps are area-
 290 weighted (AW) mean and standard deviation. Regression statistics including reduced-major-axis
 291 linear regression equation, coefficient of variation (R^2), total number of points (N), normalized
 292 mean difference (NMD), and normalized root-mean-square difference (NRMSD) are listed at the
 293 bottom right of the scatter plots. Major source regions over land are outlined in red including: 1) the
 294 Sahara – SA, 2) Middle East – ME, and 3) Asia – AS. Major dust outflow regions over ocean are
 295 outlined in green including: 4) the Caribbean Sea – CRB, 5) the tropical Atlantic Ocean – TAT, 6) the
 296 Mediterranean Sea – MED, 7) the Arabian Sea – ARB, 8) the tropical Indian Ocean and the Bay of
 297 Bengal – IND, and 9) the northwestern Pacific Ocean – NWP.



298

299 Figure 3. Comparisons of the annual extinction vertical profile normalized by total column aerosol
 300 optical depth from the Base simulation in the year of 2018 against the 15-year (2007 to 2021)
 301 climatological mean extinction vertical profile from the CALIOP over different regions including the
 302 major dust source regions over land of the Sahara – SA, Middle East – ME, and Asia – AS, and the
 303 major dust outflow regions over ocean of the Caribbean Sea – CRB, the tropical Atlantic Ocean –
 304 TAT, the Mediterranean Sea – MED, the Arabian Sea – ARB, the tropical Indian Ocean and the Bay of
 305 Bengal – IND, and the northwestern Pacific Ocean – NWP.



306 4 Model revisions to reduce the overestimation of surface fine mineral dust

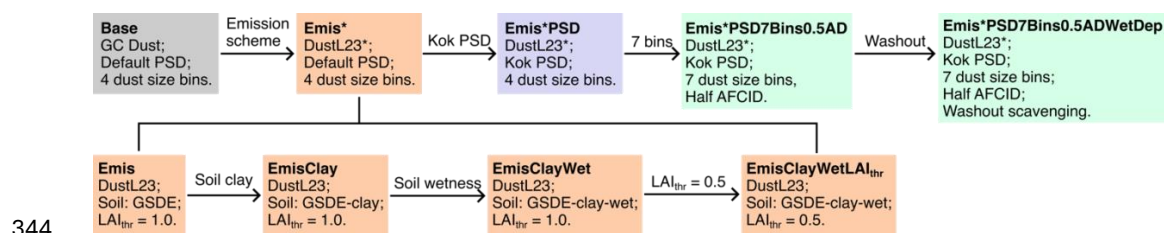
307 To reduce the overestimation of surface $PM_{2.5}$ dust, we 1) implement a new dust emission scheme
 308 with further refinements for soil properties including the clay content and soil wetness in the top
 309 soil layer and the threshold of leaf area index, 2) revisit the size distribution of emitted dust, 3)
 310 explicitly track dust with geometric diameter less than $2\ \mu m$ in four size bins, and 4) update the
 311 parametrization for size-resolved below-cloud scavenging.

312 4.1 Sensitivity simulation setup

313 Figure 4 summarizes the setup of sensitivity simulations to evaluate the effects of algorithmic
 314 modifications and their performance versus satellite-retrieved AOD and surface dust
 315 measurements. The default dust simulation (Base) in GEOS-Chem as implemented by Fairlie et al.
 316 (2007) uses the DEAD emission scheme (Zender et al., 2003) with a topographical source function
 317 (Ginoux et al., 2001; Meng et al., 2021) for natural dust (GC Dust) with 4 dust size bins for emission,
 318 transport and removal with 7 dust size bins for dust optical depth calculation and heterogeneous
 319 chemistry. To improve the spatial distributions of dust total column abundance, we implement a
 320 new dust emission scheme developed by Leung et al. (2023) (DustL23; Emis). Additional
 321 modifications on top of the original DustL23 emission scheme include 1) reducing the sensitivity of
 322 soil clay content by eliminating the multiplication of the factor of the capped soil clay content f'_{clay}
 323 (EmisClay); 2) halving the topmost soil wetness in the layer of 0-5 cm to approximate the soil
 324 wetness in the top 1-2 cm layer which is most pertinent to dust emissions (Darmenova et al., 2009;
 325 Wu et al., 2022) (EmisClayWet); and 3) reducing the threshold of LAI_{thr} from $1.0\ m^2\ m^{-2}$ to $0.5\ m^2\ m^{-2}$
 326 (EmisClayWet LAI_{thr} or Emis*). To further improve the surface fine dust simulation, we update the
 327 GEOS-Chem particle size distribution (PSD) with the PSD developed by Kok et al. (2011)
 328 (Emis*PSD) with a larger value for the side crack propagation length of λ which reduced the mass
 329 fraction of emitted fine dust. The Kok PSD was shown to have excellent agreement versus various
 330 soil size measurements (Kok, 2011), especially for fine dust distributions (González-Flórez et al.,
 331 2023). Lastly, we allow for the four dust bins with geometric diameter less than $2\ \mu m$ to have
 332 separate emission, transport, and dry and wet deposition while halving anthropogenic dust
 333 emissions from AFCID (Emis*PSD7Bins0.5AD), and with updated below-cloud or washout
 334 scavenging parametrization (Emis*PSD7Bins0.5ADWetDep). Each of these changes is examined
 335 below.



336 The total global annual source strength for each sensitivity simulation is scaled to achieve unity
 337 slope versus Deep Blue AOD (Figure A1) over major dust source regions. The surface $PM_{2.5}$ dust
 338 concentrations are calculated by accounting for aerodynamic diameter and inlet penetration
 339 efficiency (Section 2.5) as 0.676 DST1 for 4-bin simulations, and DSTbin1 + DSTbin2 + DSTbin3 +
 340 0.546 DSTbin4 for 7-bin simulations. We focus our evaluation on the skill in representing in situ
 341 $PM_{2.5}$ dust concentrations measured by SPARTAN, and in representing the spatial variation in
 342 annual mean AOD. Regression equations are calculated using reduced-major-axis linear
 343 regression.



345 Figure 4. Sensitivity simulation setup. The grey box indicates default settings with the default dust
 346 emission scheme used in GEOS-Chem (GC Dust) with 4 dust size bins (Base). The orange box
 347 indicates the implementation of a modified dust scheme based on DustL23 (Emis*). Modifications
 348 based on the original DustL23 scheme with the soil texture dataset from the Global Soil Dataset for
 349 use in Earth System Models (GSDE) (Emis) include the soil clay content (EmisClay), soil wetness
 350 (EmisClayWet), and threshold leaf area index (EmisClayWetLAI_{thr}). The simulation setup for
 351 EmisClayWetLAI_{thr} is the same as that for Emis*. The blue box indicates the modification of size
 352 distribution of emitted dust (Emis*PSD). The green boxes indicate the improvements for fine dust
 353 including explicit tracking of dust with diameter less than 2 μm with a total of 7 dust size bins with
 354 halved anthropogenic fugitive, combustion, and industrial dust (AFCID) emissions
 355 (Emis*PSD7Bins0.5AD), and updating below-cloud (washout) scavenging coefficients
 356 (Emis*PSD7Bins0.5ADWetDep).

357 4.2 Improving the spatial distribution of mineral dust with updated emission scheme

358 We implement into GEOS-Chem a new physics-based dust emission scheme developed by Leung
 359 et al. (2023) (DustL23) to replace the default dust emission scheme (Section 2.3) used in GEOS-
 360 Chem (GC Dust). The spatial distributions of DustL23 in the Community Earth System Model
 361 version 2 (CESM2) exhibited better correlation against dust optical depth datasets and AERONET



362 AOD than the DEAD scheme (Leung et al., 2024). We modify DustL23 for implementation into
 363 GEOS-Chem by 1) reducing dust emissions over wet, snow, and vegetation covered surface of
 364 semi-arid regions using Equation (7) below, 2) eliminating the multiplication of the capped clay
 365 content of the topsoil in Equation (8) below, 3) halving the soil wetness in the layer of 0-5 cm to
 366 represent the soil wetness in the top 1-2 cm layer which is most pertinent to dust emissions
 367 (Darmenova et al., 2009; Wu et al., 2022), 4) applying a regional scaling factor of 0.6 over the
 368 Sahara to reduce its emissions (Equation (8)), and 5) scaling the global total emission flux to
 369 achieve unity regression slope versus Deep Blue AOD over dusty regions.

370 We begin with the formulation for total dust emission flux F_d in $\text{kg m}^{-2} \text{s}^{-1}$ following Leung et al.
 371 (2024):

$$372 \quad F_d = \eta C_{tune} C_d f_{bare} f'_{clay} \frac{\rho_a (u_{*s}^2 - u_{*it}^2)}{u_{*st}} \left(\frac{u_{*s}}{u_{*it}} \right)^\kappa \text{ for } u_{*s} > u_{*it} \quad (6)$$

373 where η is an intermittency factor, C_{tune} is a global tuning factor for the emission strength, C_d is the
 374 time-varying soil erodibility coefficient, f_{bare} is the bare ground fraction, f'_{clay} is the clay content in
 375 the topmost soil layer of f_{clay} capped at 0.2, ρ_a is the surface air density in kg m^{-3} , u_{*s} is the soil
 376 surface friction velocity in m s^{-1} corrected from the surface friction velocity of u_* by the drag
 377 partitioning effects of F_{eff} , u_{*it} is the dynamic or impact threshold friction velocity in m s^{-1} , u_{*st} is
 378 the standardized wet fluid threshold friction velocity in m s^{-1} , and κ is the fragmentation exponent.
 379 Note that we use u_{*st} in the denominator of Equation (6) following Kok et al. (2014) instead of u_{*it}
 380 following Leung et al. (2023) for tuning purpose. The parametrization details for these factors
 381 following Leung et al. (2023) can be found in Appendix Section A3.

382 We modify the DustL23 scheme (Leung et al., 2023) by adopting the equation for the bare ground
 383 fraction in Zender et al. (2003) to reduce dust emissions over wet, snow and vegetation covered
 384 surfaces with the dry erodible land fraction taken from satellite-based land cover:

$$385 \quad f_{bare} = A_{erod} (1 - A_{snow}) \left(1 - \frac{\text{LAI}}{\text{LAI}_{thr}} \right) \quad (7)$$

386 where A_{erod} is the area fraction of erodible surfaces including barren and sparsely vegetated land
 387 cover taken from the MODIS Land Cover Climate Modeling Grid (CMG) (MCD12C1) Version 6.1 data
 388 product; A_{snow} is the area fraction of snow cover, LAI is the leaf area index (Yuan et al., 2011), and



389 LAI_{thr} is the threshold LAI to reduce the bare soil fraction due to vegetation cover. We set an
 390 intermediate value of LAI_{thr} = 0.5 m² m⁻² instead of 1.0 m² m⁻² in Leung et al. (2023) to represent
 391 the reduction in dust emissions from sparse vegetation over semi-arid regions, which is more
 392 similar to the value of 0.3 used in prior work (Mahowald et al., 1999; Zender et al., 2003).

393 The enhancement factor $f_m \geq 1$ for the wet fluid threshold friction velocity due to soil wetness is
 394 calculated using Equations (A8) and (A9), but with spatially varying clay content f_{clay} in the top soil
 395 layer. The gridded f_{clay} dataset is taken from the Global Soil Dataset for use in Earth System
 396 Models (GSDE) with various inputs from global and regional soil database (Shangguan et al., 2014),
 397 rather than the machine-learning trained Soil Grids v2.0 dataset with very few observations over
 398 arid regions (Poggio et al., 2021) used in Leung et al. (2023). In addition, we reduce the sensitivity of
 399 dust emissions to clay content by eliminating the multiplication of the capped clay content f'_{clay} .
 400 Soil wetness is taken from the parent meteorological inputs of GEOS-FP, targeted at the top 5 cm
 401 layer, and is reduced by half to approximate the soil wetness in the top 1-2 cm layer which is most
 402 pertinent to dust emissions (Darmenova et al., 2009; Wu et al., 2022).

403 The global scaling factor C_{tune} is determined by the reduced-major-axis linear regression slope of
 404 simulated AOD versus satellite-retrieved AOD over dusty regions ($\frac{AOD_{Dust}}{AOD} > 0.5$) in this study to
 405 constrain the intensity of dust emissions, whose values corresponding to different emission
 406 schemes are listed in Table A2. Additionally, a regional scaling factor of 0.6 over the Sahara (C_{sah})
 407 and unity elsewhere is applied to reduce regionally excessive dust emissions.

408 The final formulation for dust emission flux is:

$$409 \quad F_d = \eta C_{sah} C_{tune} C_d f_{bare} \frac{\rho_a (u_{*s}^2 - u_{*it}^2)}{u_{*st}} \left(\frac{u_{*s}}{u_{*it}} \right)^\kappa \text{ for } u_{*s} > u_{*it} \quad (8)$$

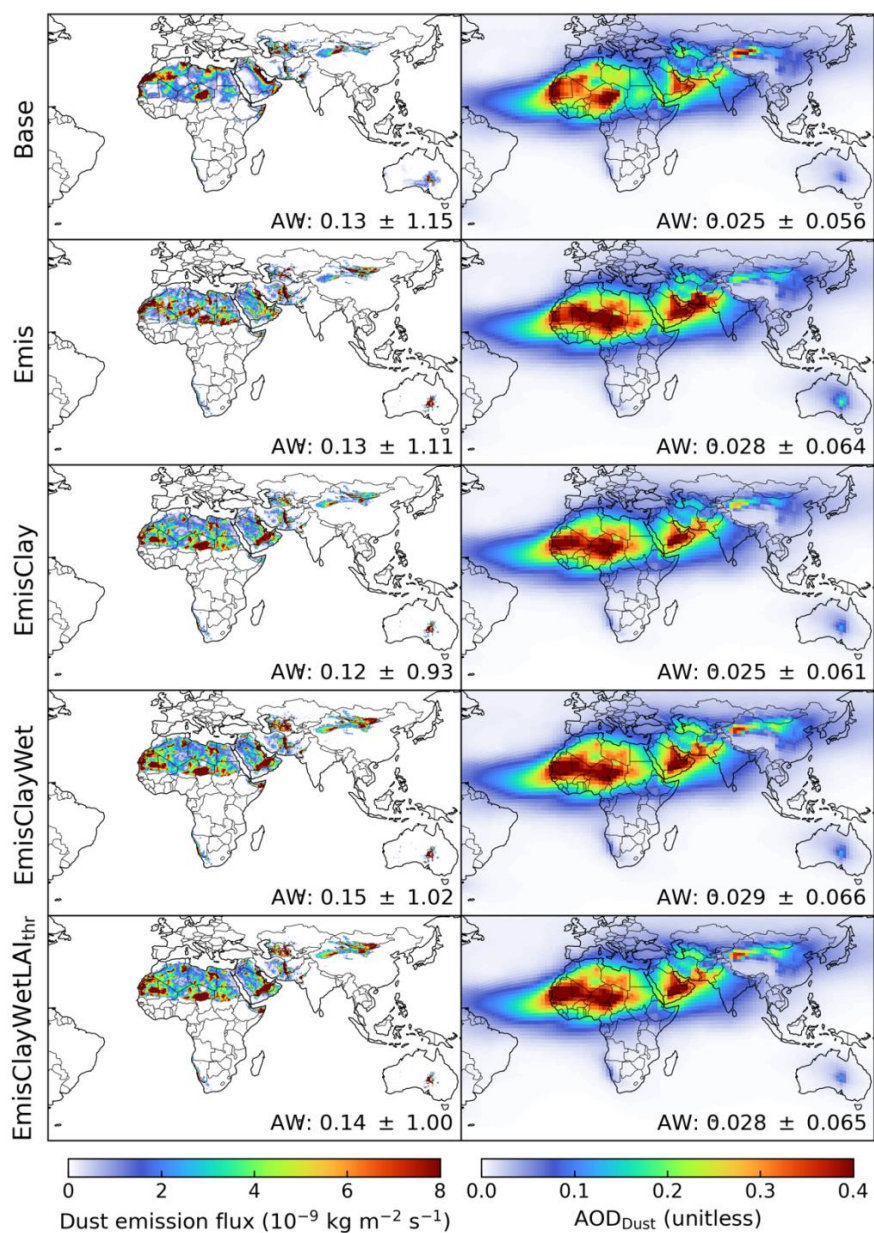
410 The calculated offline dust emissions at $0.25^\circ \times 0.3125^\circ$ resolution using Equation (8) are then used
 411 to drive GCHP simulations at C48 resolution. The spatial distributions predicted from different
 412 emission schemes are evaluated against satellite-based Deep Blue AOD, ground-based AERONET
 413 AOD, and SPARTAN surface PM_{2.5} dust measurements.

414 Figure 5 shows the spatial distributions of annual dust emission fluxes and dust optical depth
 415 predicted from different emission schemes, with Figure 6 showing the comparisons against Deep



Blue satellite AOD globally and over major dust source regions. Comparison of the Base and Emis schemes reveals that the latter captures more secondary dust emission spots, especially over the Sahara, and inland dust sources in Saudi Arabia. However, the comparison against Deep Blue AOD over the Sahara is degraded versus the default scheme (Figure 6). As suggested by prior studies, soil clay content is an important factor affecting the threshold friction velocity (Fécan et al., 1999; Tian et al., 2021; Zender et al., 2003) and sandblasting efficiency (Zender et al., 2003), and is often tuned for the optimization of dust emissions (Leung et al., 2024; Tian et al., 2021). Eliminating the multiplication of the capped clay content of f'_{clay} reduces the dust emission sensitivity to the clay content, increasing emissions from the Bodélé Depression in Chad and El Djouf across the border of Mauritania and Mali over the Sahara, from the Rub' al Khali desert in the inland Saudi Arabi, and Taklamakan desert in the northwest China (Figure 5, EmisClay). Correspondingly, the R^2 from the linear regression against Deep Blue AOD is improved from 0.60 to 0.70 over the Sahara, from 0.68 to 0.77 over the Middle East, and from 0.35 to 0.56 over Asia (Figure 6). The other two modifications of halving soil wetness (EmisClayWet) and setting LAI_{thr} to $0.5 \text{ m}^2 \text{ m}^{-2}$ (EmisClayWet LAI_{thr}) slightly improve the spatial distribution of dust emissions by reducing the underestimation in Asia while retaining the agreements in the Sahara and Middle East (Figure 6). Using the same dusty region of the EmisClayWet LAI_{thr} scheme for the comparisons of all dust emission schemes versus Deep Blue AOD confirms similarly slight improvements of regional dust emissions (Figure A2). Together these refinements exhibit comparable global performance as the Base simulation versus Deep Blue AOD with improvements to the relative regional magnitude of dust across the Sahara, Middle East and Asia.

Figure 7 shows the evaluation of the Emis* (or EmisClayWet LAI_{thr}) simulation with ground-based observations from AERONET and SPARTAN. The overestimation of surface $PM_{2.5}$ dust against the ground-based measurements of SPARTAN is reduced from 73% (Figure 2) to 37% (Figure 7), reflecting regional improvements of the spatial distributions especially over the Middle East (Figure 6). The skill in representing AOD in the Emis* simulation remains comparable to that in the Base simulation shown in Figure 2.



443

444 Figure 5. Annual dust emission flux (left) and simulated dust optical depth (AOD_{Dust}; right) in the
 445 year of 2018 zoomed in over dusty regions of the Sahara, Middle East, and Asia from different
 446 emission schemes as described in Figure 4. Inset values are area-weighted (AW) mean and
 447 standard deviation globally.

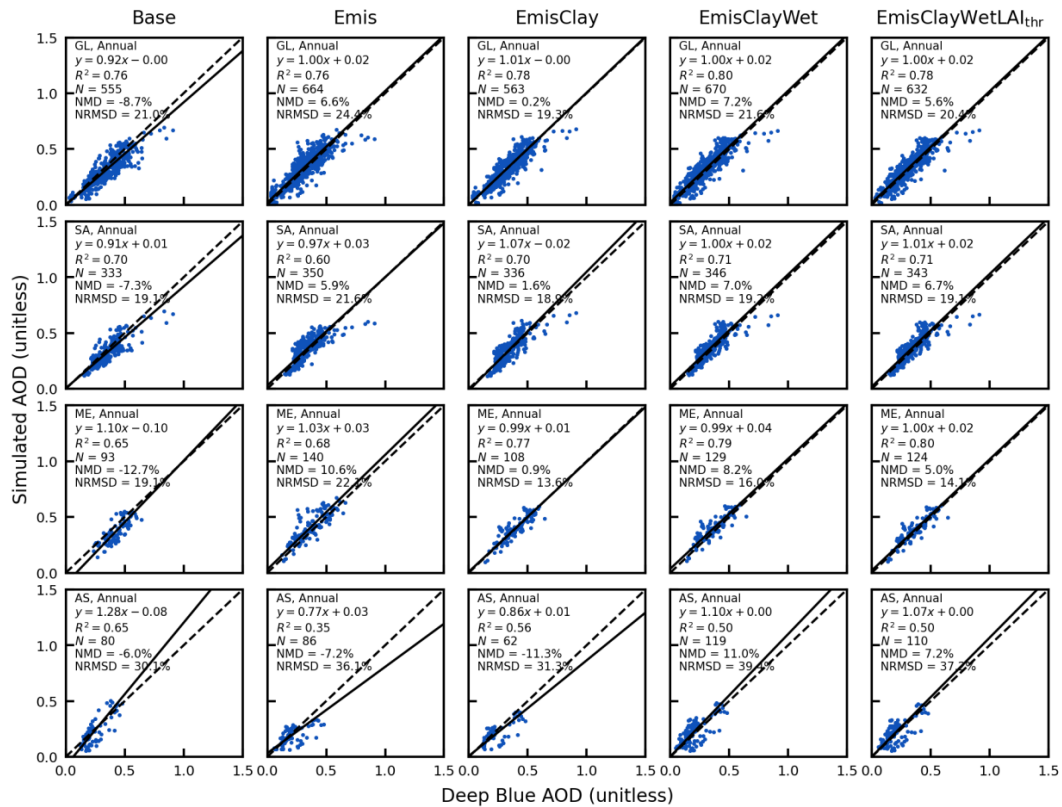
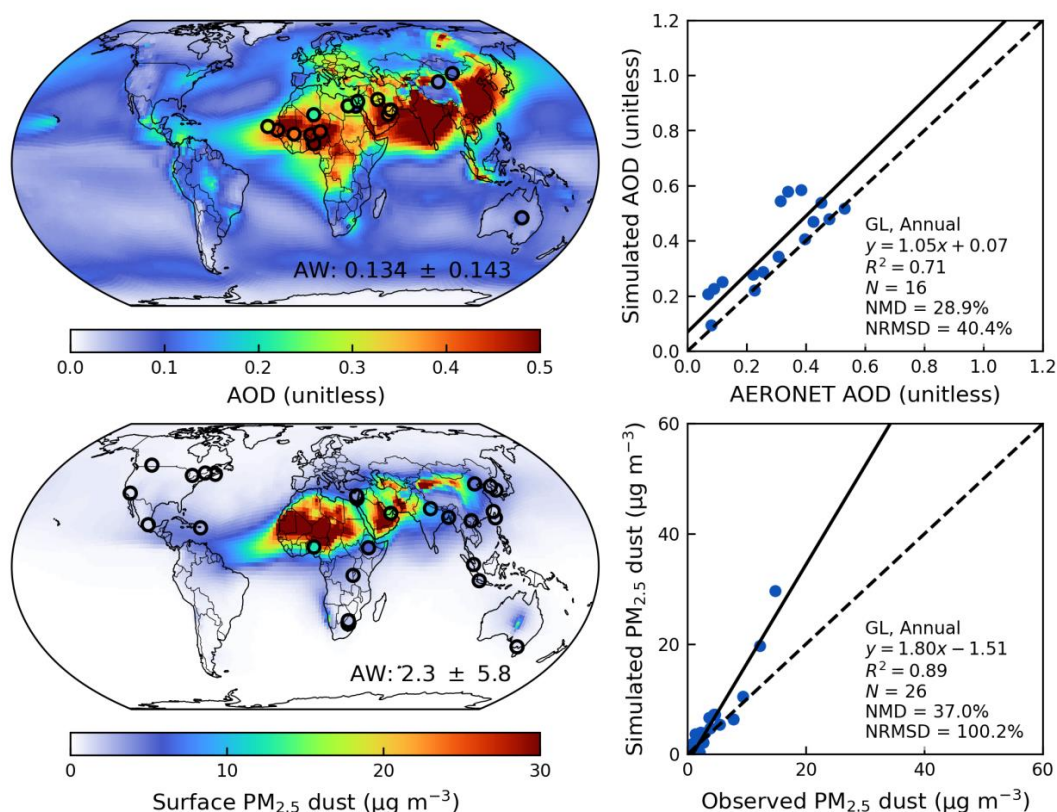


Figure 6. Comparisons of annual simulated aerosol optical depth (AOD) versus the Deep Blue satellite AOD globally (GL) and over main dust source regions of the Sahara – SA, Middle East – ME, and Asia (AS) with different emission schemes. Regression statistics including reduced-major-axis linear regression equation, coefficient of variation (R^2), total number of points (N), normalized mean difference (NMD), and normalized root-mean-square difference (NRMSD) are in the top left.



454

455 Figure 7. Annual simulated aerosol optical depth (AOD) and comparison against ground-based
 456 observations from the AERONET over dusty regions ($AOD_{Dust}/AOD > 0.5$) (top); Annual simulated
 457 surface PM_{2.5} dust and comparison against ground-based measurements from the SPARTAN from
 458 the Emis* simulation in the year of 2018 (bottom). Filled circles on the maps represent ground-
 459 based observations from SPARTAN and AERONET. Inset values at the bottom right of the maps are
 460 area-weighted (AW) mean and standard deviation. Regression statistics including the reduced-
 461 major-axis linear regression equation, coefficient of variation (R^2), total number of points (N),
 462 normalized mean difference (NMD), and normalized root-mean-square difference (NRMSD) are
 463 listed at the bottom right of the scatter plots.

464 4.3 Improving the representation of fine mineral dust

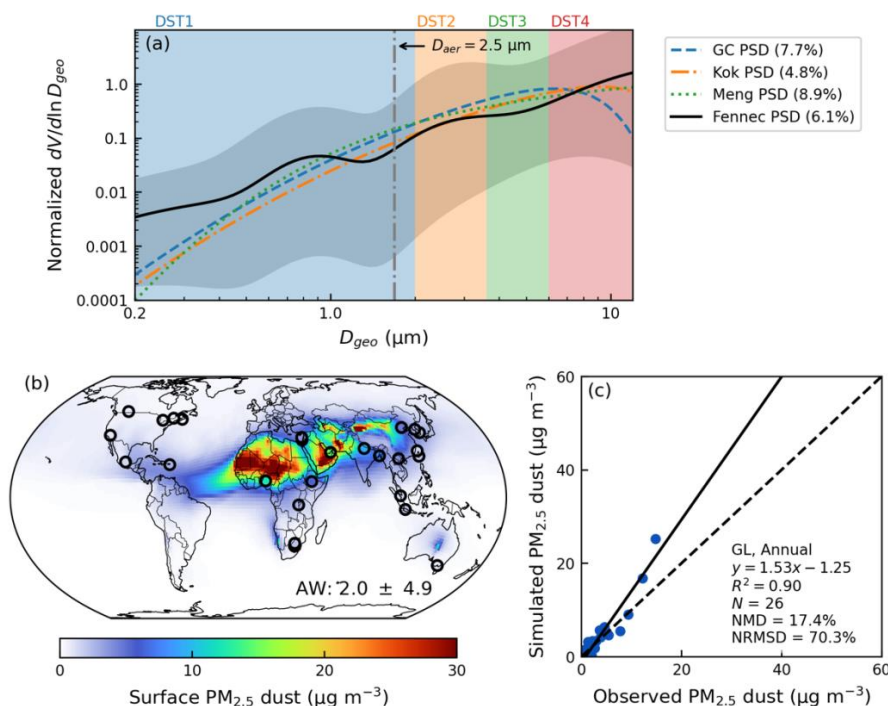
465 As the size distribution of mineral dust is particularly important for the performance discrepancy
 466 between simulated AOD over dusty regions and surface PM_{2.5} dust, we focus on improving its size-



467 resolved source and sink.

468 4.3.1 Revisiting the size distribution of emitted mineral dust

469 Figure 8a shows different PSDs including the default PSD used in the GEOS-Chem (GC PSD) based
 470 on the brittle fragmentation theory with the side crack propagation length λ of 8 μm (Zhang et al.,
 471 2013), the Kok PSD with λ of 12 μm (Kok, 2011), and the Meng PSD focusing on the optimization for
 472 coarse to super coarse dust (Meng et al., 2022), in comparison with the observed PSD from the
 473 2011 Fennec campaign (Ryder et al., 2013). While all modelled PSDs are within the wide range of
 474 PSD from the Fennec campaign, the fraction of emitted DST1 from the Kok PSD exhibits greater
 475 consistency with the Fennec observations than the other two PSDs. Larger discrepancy for the size
 476 distribution with diameter less than $\sim 0.4 \mu\text{m}$ between the observed PSD from Fennec and
 477 parametrized PSDs is possibly due to anthropogenic aerosol influence (González-Flórez et al.,
 478 2023). In addition, a recent field study in the Moroccan Sahara (González-Flórez et al., 2023)
 479 indicated overall agreement of emitted dust size distributions against the Kok PSD especially at the
 480 fine diameter range. Therefore, we adopt the Kok PSD for the size distribution of emitted mineral
 481 dust in GEOS-Chem. Figure 8b shows the spatial distribution from the Emis*PSD simulation which
 482 remains similar to that from the Emis* simulation in Figure 7. Reduced emissions from DST1 by
 483 using the Kok PSD reduces the overestimation of surface $\text{PM}_{2.5}$ dust from 37% to 17% compared to
 484 the ground-based measurements from SPARTAN (Figure 8c).



485

486 Figure 8. a) Normalized particle size distribution (PSD) of emitted dust based on default PSD used
 487 in GEOS-Chem (GC PSD) (Zhang et al., 2013), the Kok PSD (Kok, 2011), the Meng PSD (Meng et al.,
 488 2022), and the Fennec PSD (Ryder et al., 2013). All PSDs are normalized for a total volumetric
 489 integration of 1 within the diameter range of $0.2 \mu\text{m}$ to $12 \mu\text{m}$ used in GEOS-Chem. The grey shades
 490 show the minimum and maximum PSD curves from the Fennec 2011 campaign. Grey dash-dotted
 491 line indicates the corresponding geometric diameter of $1.7 \mu\text{m}$ for the aerodynamic diameter of 2.5
 492 μm . Filled rectangles indicate size ranges of 4 dust size bins. Percentages adjacent to each PSD are
 493 mass fractions of emitted DST1 over total dust emission flux within diameter range of $0.2 \mu\text{m}$ to 12
 494 μm . b) Simulated annual surface $\text{PM}_{2.5}$ dust from the Emis*PSD simulation in the year of 2018.
 495 Filled circles on the map represent ground-based observations from SPARTAN and AERONET. Inset
 496 values at the bottom right of the maps are area-weighted (AW) mean and standard deviation. c)
 497 Comparison of simulated $\text{PM}_{2.5}$ dust versus observed fine dust from SPARTAN. Regression
 498 statistics including the reduced-major-axis linear regression equation, coefficient of variation (R^2),
 499 total number of points (N), normalized mean difference (NMD), and normalized root-mean-square
 500 difference (NRMSD) are listed at the bottom right.



4.3.2 Improving the size-resolved dry and wet deposition of mineral dust

The default below-cloud (washout) scavenging of dust by rain and snow in GEOS-Chem is separated for fine (DST1) and coarse dust (DST2 to DST4) (Wang et al., 2011). However, washout scavenging coefficients strongly depend on aerosol size, varying by 3 orders of magnitude for diameter ranging from 1 to 10 μm (Wang et al., 2014b). To improve the size-dependent washout treatment of dust, we update washout rates by rain and snow for 7 dust size bins by (Wang et al., 2014b):

$$\Lambda = A(D_d) \left(\frac{P_d}{f_r} \right)^{B(D_d)} \quad (9)$$

where Λ is the washout scavenging coefficient in s^{-1} by either rain or snow; P_d is the precipitation rate in mm h^{-1} falling from upper layers; f_r is the area fraction of precipitation within each grid box; A and B are empirical constants dependent on dust size D_d . Using the same equations for A and B as Wang et al. (2014b), the updated values for different dust size bins are summarized in Table 2.

Table 2. Values of A and B for washout parametrizations by rain and snow for different dust size bins.

Diameter (μm)	Rain ($T \geq 268 \text{ K}$)		Snow ($248 \text{ K} \leq T < 268 \text{ K}$)	
	A	B	A	B
Bin1 (0.2–0.36)	4.0×10^{-7}	0.71	7.3×10^{-6}	0.57
Bin2 (0.36–0.6)	4.1×10^{-7}	0.71	1.3×10^{-5}	0.56
Bin3 (0.6–1.2)	4.8×10^{-7}	0.72	2.7×10^{-5}	0.56
Bin4 (1.2–2.0)	8.4×10^{-7}	0.73	6.0×10^{-5}	0.55
Bin5 (2.0–3.6)	4.8×10^{-5}	0.88	4.2×10^{-4}	0.61
Bin6 (3.6–6.0)	2.2×10^{-4}	0.87	1.3×10^{-3}	0.67
Bin7 (6.0–12.0)	3.4×10^{-4}	0.84	2.4×10^{-3}	0.73

Figure 9 shows the size-dependent variations of mineral dust dry and wet deposition. The dry deposition velocity can vary by a factor of 4.9 among Bin1 to Bin4 with the minimum near the geometric diameter of 0.5 μm . The washout scavenging coefficient can vary by a factor of 2.6 among Bin1 to Bin4 with the minimum near the geometric diameter of 0.4 μm . Given the steep



520 increasing strength of emitted dust from Bin1 to Bin4 (Figure 8), there is need to explicitly track dust
 521 within DST1. We evaluate these developments by examining their effects on the fractional
 522 contributions of fine dust to total dust.

523 Figure 10 shows the fractional contributions of fine dust with geometric diameter less than $2\ \mu\text{m}$ to
 524 total dust ($\text{AOD}_{\text{FineDust}}/\text{AOD}_{\text{Dust}}$) from the simulations with a total of 7 dust bins for dry deposition
 525 with updated washout scavenging parametrization and their differences. Due to the dominance of
 526 dry deposition over arid dusty regions, the explicit tracking of fine dust dry deposition slightly
 527 reduces $\text{AOD}_{\text{FineDust}}/\text{AOD}_{\text{Dust}}$ over major dust source regions. However, the anthropogenic
 528 contributions to fine dust are correspondingly enhanced over urban and industrial regions, leading
 529 to degraded comparison against SPARTAN measurements (Figure A3). We thus scale the AFCID
 530 emissions by half to reduce the excessive contributions from this uncertain source
 531 ($\text{Emis} \cdot \text{PSD7Bins} \cdot 0.5\text{AD}$). In addition, accounting for the steep washout scavenging efficiency across
 532 DSTbin5 to DSTbin7 (Figure 9) with updated washout parametrization would induce enhanced
 533 fractional contributions especially for DSTbin5 (Figure A4) and thus relatively reduce fractional
 534 contributions from fine dust with geometric diameter less than $2\ \mu\text{m}$ to total dust
 535 ($\text{AOD}_{\text{FineDust}}/\text{AOD}_{\text{Dust}}$). Figure 11 shows the overall performance with all revisions from the
 536 simulation of $\text{Emis} \cdot \text{PSD7Bins} \cdot 0.5\text{ADWetDep}$. The reduced-major-axis linear regression slope is
 537 further reduced from 1.53 (Figure 8) to 1.44 with comparable values of NMD against SPARTAN
 538 measurements.

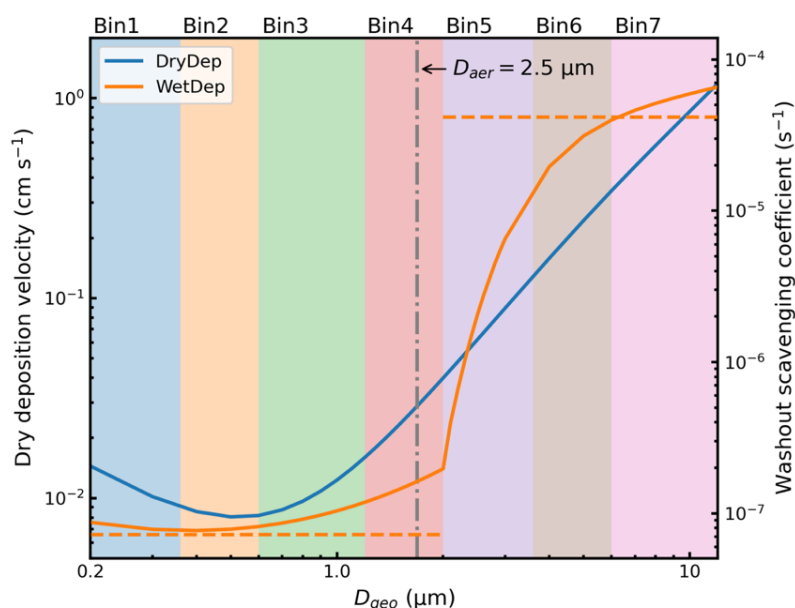
539 Comparisons against other surface dust datasets also show improved or comparable performance
 540 compared to the Base simulation. Figure A5 shows the comparison against ground-observations
 541 over North America. Using the refined new dust emission scheme with the replacement of the size
 542 distribution from the Kok PSD, explicitly tracking submicron bins for dry deposition, and updating
 543 the washout scavenging parametrization contribute to a comparable extent to reduce the
 544 overestimation over North America from 43% of the Base simulation to 15% of the
 545 $\text{Emis} \cdot \text{PSD7Bins} \cdot 0.5\text{ADWetDep}$ simulation. Comparisons against surface concentrations and total
 546 deposition of PM_{10} dust (Li et al., 2022b) for the $\text{Emis} \cdot \text{PSD7Bins} \cdot 0.5\text{ADWetDep}$ simulation are also
 547 comparable with the Base simulation (Figures A6 and A7). Consistent with prior studies (Leung et
 548 al., 2023; Meng et al., 2021), fine-resolution meteorological fields are needed to capture dust
 549 emission hotspots. The simulated total column AOD would be underestimated by 14% compared
 550 to AERONET, and the surface fine dust would be underestimated by 22% compared to SPARTAN if



551 the dust emissions are calculated with meteorological fields at C48 resolution (Figure A8). Overall
 552 comparisons for the seasonal mean between the Base and the Emis*PSD7Bins0.5ADWetDep
 553 simulations confirm largely reduced overestimation for the surface fine dust against SPARTAN,
 554 while retaining comparable skill for the total column AOD against AERONET (Figures A9 to A12).

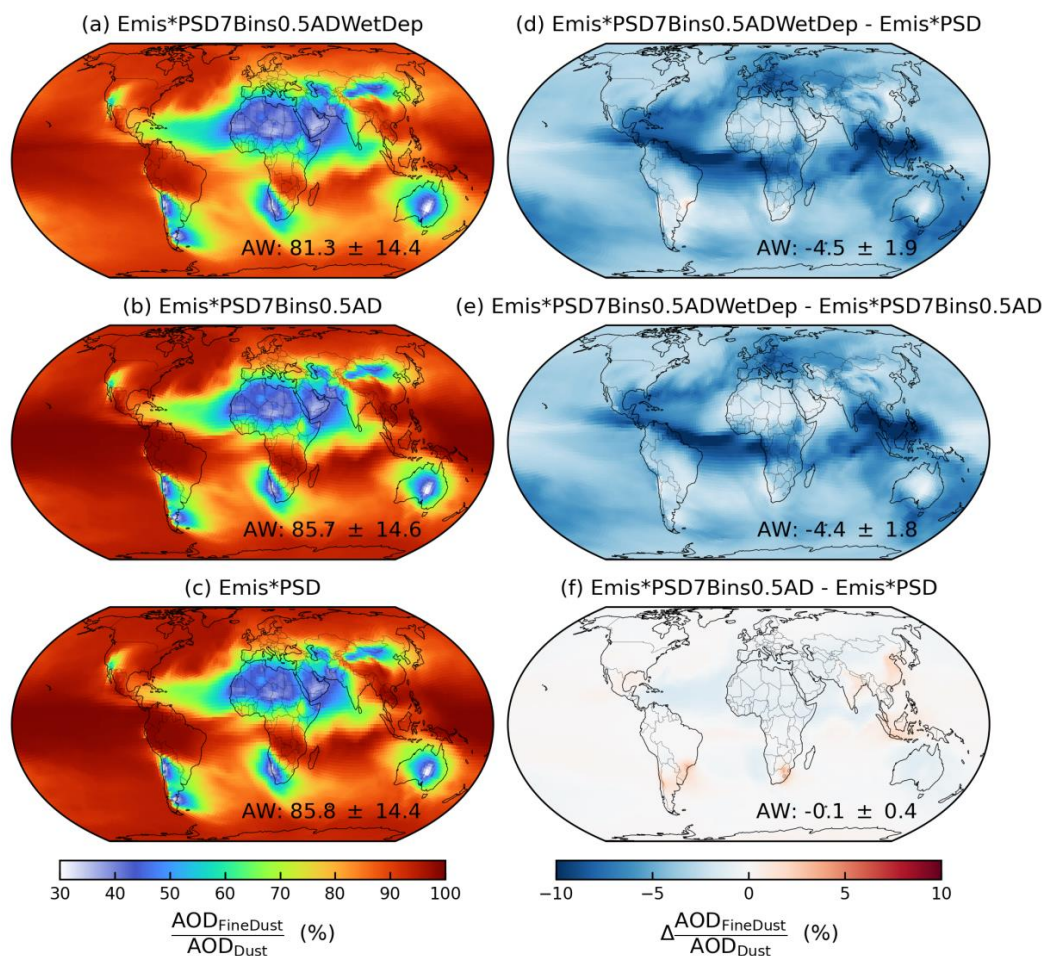
555 Table 3 summarizes the effects of different modifications on the model performance of total
 556 column AOD and surface fine mineral dust in this study. Strong overestimation of surface $PM_{2.5}$
 557 dust concentrations exist in the Base simulation by a factor of 2.2 versus SPARTAN measured dust.
 558 Updating the dust emission scheme with further refinements in the soil properties reduces the
 559 overestimation of surface $PM_{2.5}$ dust by 36%. The surface overestimation by 37% is reduced to 21%
 560 by updating the size distribution of emitted dust, explicitly tracking dust with diameter less than 2
 561 μm in 4 bins, and updating the parametrization of below-cloud scavenging. The comparisons of
 562 simulated AOD versus AERONET and Deep Blue AOD are comparable for all simulations with the
 563 correlation coefficient of 0.8-0.9, and NMDs from -9% to 31%. The emissions between the Base
 564 and Emis* simulations are comparable with the global annual dust emission of $\sim 2000 \text{ Tg yr}^{-1}$, which
 565 is within the range of 1000-5000 Tg yr^{-1} from intercomparison projects (Huneeus et al., 2011; Wu et
 566 al., 2020). As the Kok PSD reduces the mass fraction of fine dust, the total emitted mass is
 567 enhanced to $\sim 3000 \text{ Tg yr}^{-1}$ with larger contributions from coarse dust.

568



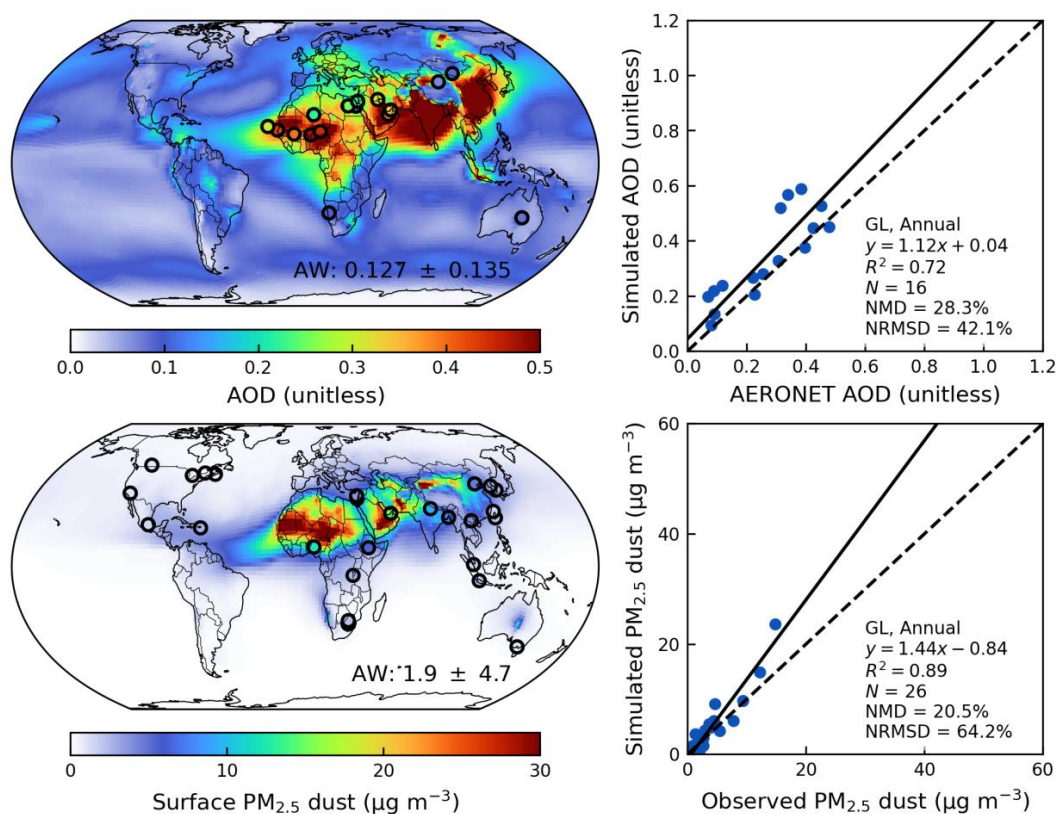
569

570 Figure 9. Size-resolved dry deposition velocity over desert (left y-axis) and washout scavenging
 571 coefficient by rain (right y-axis). Dry deposition velocity is calculated with the friction velocity of 0.4
 572 m s^{-1} and the particle density of 2500 kg m^{-3} with the default dry deposition scheme used in the
 573 GEOS-Chem. Washout scavenging coefficient is calculated with the precipitation rate of 0.1
 574 mm h^{-1} with the updated washout parametrization. Orange horizontal dash lines indicate the
 575 default washout scavenging coefficients by rain with the precipitation rate of 0.1 mm h^{-1} for fine
 576 aerosol (Bin1 to Bin4) and coarse aerosol (Bin5 to Bin7). Grey dash-dotted line indicates the
 577 corresponding geometric diameter of 1.7 μm for the aerodynamic diameter of 2.5 μm . Filled
 578 rectangles indicate different simulated dust size bins.



579

580 Figure 10. Fractional contributions of fine dust with geometric diameter less than 2 μm to total dust
 581 column abundance ($\text{AOD}_{\text{FineDust}}/\text{AOD}_{\text{Dust}}$) from the a) Emis*PSD7Bins0.5ADWetDep, b)
 582 Emis*PSD7Bins0.5AD, c) Emis*PSD and their absolute differences. Inset values at the bottom right
 583 are area-weighted (AW) mean and standard deviation.



584

585 Figure 11. Annual simulated aerosol optical depth (AOD) and comparison against ground-based
 586 observations from AERONET over dusty regions ($AOD_{Dust}/AOD > 0.5$) (top); Annual simulated
 587 surface PM_{2.5} dust and comparison against ground-based measurements from SPARTAN from the
 588 Emis*PSD7Bins0.5ADWetDep simulation in the year of 2018 (bottom). Filled circles on the maps
 589 represent ground-based observations from SPARTAN and AERONET. Inset values at the bottom
 590 right of the maps are area-weighted (AW) mean and standard deviation. Regression statistics
 591 including the reduced-major-axis linear regression equation, R^2 , total number of points (N),
 592 normalized mean difference (NMD), and normalized root-mean-square difference (NRMSD) are
 593 listed at the bottom right of the scatter plots.

594

595 Table 3. Effects of different modifications on the model performance of simulated annual surface $PM_{2.5}$ dust versus SPARTAN, and
596 simulated annual aerosol optical depth (AOD) versus AERONET AOD and Deep Blue satellite AOD in terms of the correlation coefficient
597 (r), the reduced-major-axis linear regression slope, and the normalized mean difference (NMD), with associated total annual dust
598 emissions in the year of 2018.

Simulation	Simulated surface PM _{2.5} dust versus SPARTAN			Simulated AOD versus						Emissions (Tg yr ⁻¹)
	AERONET AOD			Deep Blue AOD						
	<i>r</i>	slope	NMD (%)	<i>r</i>	slope	NMD (%)	<i>r</i>	slope	NMD (%)	
Base	0.95	2.20	73.2	0.84	1.02	17.7	0.87	0.92	-8.7	2025
Emis*										
Emis	0.96	1.79	47.7	0.85	1.10	26.2	0.87	1.00	6.6	2128
EmisClay	0.95	1.69	18.1	0.86	1.05	23.7	0.88	1.01	0.2	1954
EmisClayWet	0.94	1.84	44.3	0.87	1.11	30.7	0.89	1.00	7.2	2376
EmisClayWetLA _{1hr}	0.95	1.80	37.0	0.85	1.05	28.9	0.88	1.00	5.6	2262
Emis*PSD	0.95	1.53	17.4	0.83	1.12	29.7	0.89	1.00	4.3	3069
Emis*PSD7Bins0.5AD	0.94	1.48	25.3	0.85	1.12	28.3	0.89	1.00	3.2	2952
Emis*PSD7Bins0.5ADWetDep	0.95	1.44	20.5	0.83	1.11	28.7	0.89	1.00	3.6	2943



600 5 Conclusions

601 In summary, we evaluate and improve the mineral dust simulation in the GEOS-Chem model by
602 building upon recent ground-based measurements from SPARTAN of mineral dust in $PM_{2.5}$ over
603 land, together with total column AOD from AERONET measurements and from MODIS and VIIRS
604 Deep Blue satellite product. We devote attention to the representation of aerodynamic diameter
605 when comparing with ground-based $PM_{2.5}$ measurements, since representation as geometric
606 diameter in models would introduce two-fold bias. We nonetheless find that the standard GEOS-
607 Chem chemical transport model much better represents columnar AOD with a slope near unity
608 than surface $PM_{2.5}$ dust concentrations which are overestimated by a factor of two. Comparison of
609 simulated extinction profile versus the 15-year climatological CALIOP extinction profile yields
610 overall consistency in the vertical shape (Figure 3), indicating the importance of other dominant
611 factors.

612 We develop the mineral dust representation in GEOS-Chem with attention to its sources, size
613 distribution, and sinks. We implement a new dust emission scheme based on Leung et al. (2023)
614 with further refinements to the clay content and wetness in the topsoil layer, threshold leaf area
615 index, and reducing dust emissions over snow and vegetation covered land surfaces. The NMD
616 versus surface measurements is reduced by 36% while the simulated AOD better represents the
617 spatial distribution of Deep Blue AOD over dusty regions. To further improve the fine dust
618 representation in GEOS-Chem, we revisit the size distribution of emitted dust and find the Kok
619 particle size distribution (PSD; Kok, 2011) better represents the mass fraction of fine dust
620 measured during the Fennec field campaign over Northern Africa than the default PSD and that its
621 implementation into GEOS-Chem reduces the surface overestimation of $PM_{2.5}$ dust by 20%. We
622 also enable explicit tracking of mineral dust with geometric diameter less than $2\ \mu m$ in 4 size bins
623 for emission, transport, and deposition with updated parametrization for below-cloud scavenging,
624 which further reduces the overestimation of surface $PM_{2.5}$ dust concentrations to within 21%.

625 These investigations indicate the importance of size type reconciliation in models versus
626 measurements, the spatial distribution of dust emissions, the size distribution of emitted dust, and
627 the explicit tracking of fine dust bins for more accurate simulation of fine dust abundance from the
628 surface to the column.



Appendix A: Additional details about dust emission parametrizations, SPARTAN dust, and complementary figures

A1. A global dust equation

We follow a global dust equation for the calculation of surface PM_{2.5} dust concentrations from SPARTAN (Liu et al., 2022):

$$\text{Dust} = [1.89\text{Al} \times (1 + \text{MAL}) + 2.14\text{Si} + 1.40\text{Ca} + 1.36\text{Fe} + 1.67\text{Ti}] \times \text{CF} \quad (\text{A1})$$

where 1.89, 2.14, 1.40, 1.36, and 1.67 are the mass conversion ratios for corresponding mineral oxides; MAL is the mineral-to-aluminum mass ratio of (K₂O + MgO + Na₂O)/Al₂O₃; CF is a correction factor (CF) to account for other missing compounds.

A2. Horizontal saltation flux in standard version of GEOS-Chem

The default horizontal saltation flux Q_s in GEOS-Chem is based on the parametrization of White (1979):

$$Q_s = C_z \frac{\rho_a}{g} u_{*s}^3 \left(1 - \frac{u_{*ft}}{u_{*s}}\right) \left(1 + \frac{u_{*ft}}{u_{*s}}\right)^2 \text{ for } u_{*s} > u_{*ft} \quad (\text{A2})$$

where $C_z = 2.61$ is the saltation constant; ρ_a is the air density in kg m⁻³; $g = 9.81 \text{ m s}^{-2}$ is the gravitational acceleration; the drag partitioning effects are ignored by default and thus $u_{*s} = u_*$, where u_* is calculated from the wind speed at 10 m u_{10m} based on the logarithmic wind profile within the boundary layer under adiabatic conditions (Marticorena and Bergametti, 1995):

$$u_* = \frac{k u_{10m}}{\ln(z_0/z_{0a})} \quad (\text{A3})$$

where $k = 0.4$ is the von Kármán constant; u_{10m} is the wind speed at 10 m; $z_0 = 10 \text{ m}$ is the reference height; $z_{0a} = 10^{-4} \text{ m}$ is the surface roughness height. The wet fluid threshold friction velocity of u_{*ft} is the minimum surface friction velocity required to initiate the saltation from the bare soil (Fécan et al., 1999):

$$u_{*ft} = u_{*ft0} \cdot f_m \quad (\text{A4})$$



652 where u_{*ft0} is the dry fluid threshold friction velocity following Iversen and White (1982):

$$653 \quad u_{*ft0} = \begin{cases} \frac{0.129K}{\sqrt{1.928Re^{0.092} - 1}}, & 0.03 < Re < 10 \\ 0.12K[1 - 0.0858e^{-0.0617(Re-10)}], & Re \geq 10 \end{cases} \quad (A5)$$

654 where:

$$655 \quad K = \sqrt{\frac{\rho_p g D_p}{\rho_a} \left(1 + \frac{0.006}{\rho_p g D_p^{2.5}} \right)} \quad (A6)$$

$$656 \quad Re = 1331D_p^{1.56} + 0.38 \quad (A7)$$

657 Where $D_p = 75 \mu\text{m}$ is the diameter of soil particle which corresponds to the minimum dry fluid
 658 threshold velocity of u_{*ft0} (Iversen and White, 1982).

659 The enhancement factor $f_m \geq 1$ is a function of soil wetness (Fécan et al., 1999):

$$660 \quad f_m = \begin{cases} 1, & w \leq w_t \\ \sqrt{1 + 1.21[100(w - w_t)]^{0.68}}, & w > w_t \end{cases} \quad (A8)$$

661 where w is the gravimetric soil moisture (kg kg^{-1}) in the shallowest soil layer; w_t is the threshold
 662 gravimetric water content above which u_{*ft} increases with soil wetness (Fécan et al., 1999):

$$663 \quad w_t = 0.01a (17f_{clay} + 14f_{clay}^2) \quad (A9)$$

664 where a is a tuning factor which is taken as $1/f_{clay} = 5$ by default.

665 **A3. Additional details about the new dust emission scheme**

666 The variables used in the calculation for the total dust emission flux F_d (Equation (6)) can be
 667 categorized into meteorological fields including η , ρ_a , and u_* , land surface properties including
 668 f_{bare} , f'_{clay} , F_{eff} , and u_{*it} , intrinsic soil erodibility properties including u_{*st} , C_d , and κ , and a global
 669 tuning factor of C_{tune} .

670 Intermittency effects due to the fluctuation of instantaneous soil friction velocity \tilde{u}_s are reflected in
 671 the intermittency factor of η , which is denoted by the temporal fraction of active dust emission



672 ranging from 0 to 1 within a transport time step. The parametrization of η is based on Comola et al.
 673 (2019):

$$674 \quad \eta = 1 - P_{ft} + \alpha(P_{ft} - P_{it}) \quad (A10)$$

675 where P_{ft} and P_{it} are the cumulative probability of instantaneous friction velocity larger than a wet
 676 fluid threshold, and an impact threshold, respectively; α is the fraction of \tilde{u}_s crossing a wet fluid
 677 threshold over the total fraction crossing a wet fluid threshold and an impact threshold.

678 The calculation of η is based on velocity at the saltation height of $z_{sal} = 0.1$ m. Thus the surface
 679 friction velocity of u_{*s} , and threshold velocities of u_{*ft} and u_{*it} are first calculated at the saltation
 680 height based on (Marticorena and Bergametti, 1995):

$$681 \quad u_X(sal) = \frac{u_{*X}}{k} \ln\left(\frac{z_{sal}}{z_{0a}}\right) \quad (A11)$$

682 where the subscript X can be ft , it or s , $z_{0a} = 10^{-4}$ m, and $k = 0.386$ is the von Kármán constant.

683 Assuming a normal distribution of instantaneous soil friction velocity $\tilde{u}_s \sim N(u_s, \sigma_{\tilde{u}_s}^2)$, a standard
 684 deviation of instantaneous friction velocity $\sigma_{\tilde{u}_s}$ is a central parameter to calculate the fraction of
 685 active dust emissions within a time step for transportation. $\sigma_{\tilde{u}_s}$ is calculated based on the similarity
 686 theory (Panofsky et al., 1977):

$$687 \quad \sigma_{\tilde{u}_s} = u_{*s} \left(12 - 0.5 \frac{z_i}{L}\right)^{1/3} \quad (A12)$$

688 where z_i is the planetary boundary layer height, and L is the Monin-bukhov length calculated by
 689 (Panofsky et al., 1977):

$$690 \quad L = -\frac{\rho_a c_p T u_*^3}{kgH} \quad (A13)$$

691 where $c_p = 1005 \text{ J kg}^{-1} \text{ K}^{-1}$ is the specific heat capacity of air under constant pressure; T is surface
 692 air temperature; u_* in m s^{-1} is the original surface friction velocity without the drag partitioning
 693 correction; $g = 9.81 \text{ m s}^{-2}$ is the gravitational acceleration; H is the sensible heat flux from
 694 turbulence in W m^{-2} .



695 Given that a normal distribution is assumed, cumulative probabilities of P_{ft} and P_{it} can be
 696 calculated by $P_{ft} = 0.5[1 + \operatorname{erf}(\frac{u_{ft}-u_s}{\sqrt{2}\sigma_{\tilde{u}_s}})]$, and $P_{it} = 0.5[1 + \operatorname{erf}(\frac{u_{it}-u_s}{\sqrt{2}\sigma_{\tilde{u}_s}})]$. α is the number of crossing
 697 rate of \tilde{u}_s across the wet fluid threshold C_{ft} over the total number of crossing rate of \tilde{u}_s across the
 698 wet fluid threshold C_{ft} and the impact threshold C_{it} (Comola et al., 2019):

$$699 \quad \alpha = \frac{C_{ft}}{C_{ft} + C_{it}} \quad (A14)$$

700 The crossing fraction of α is approximated by $\alpha \approx [\exp(\frac{u_{ft}^2 - u_{it}^2 - 2u_s(u_{ft} - u_{it})}{2\sigma_{\tilde{u}_s}^2}) + 1]^{-1}$ as suggested by
 701 Comola et al. (2019).

702 The soil surface friction velocity of u_{*s} is calculated by (Leung et al., 2023; Marticorena and
 703 Bergametti, 1995; Webb et al., 2020):

$$704 \quad u_{*s} = u_* F_{eff} \quad (A15)$$

705 where u_* is the surface friction velocity taken directly from the parent meteorological fields; F_{eff} is
 706 the drag partitioning effects due to the presence of non-erodible elements including rocks and
 707 vegetation.

708 Drag partitioning effects are calculated following Leung et al. (2023):

$$709 \quad F_{eff} = (A_r f_{eff,r}^3 + A_v f_{eff,v}^3)^{1/3} \quad (A16)$$

710 where A_r is the fraction of barren and sparsely vegetated land cover approximated by A_{erod} ; A_v is
 711 the fraction of short vegetation land cover taken from the MCD12C1 Version 6.1 land cover
 712 product; $f_{eff,r}$ is the drag partitioning effects due to rocks (Marticorena and Bergametti, 1995):

$$713 \quad f_{eff,r} = 1 - \frac{\ln(\frac{z_{0a}}{z_{0s}})}{\ln\left[b_1 \left(\frac{X}{z_{0s}}\right)^{b_2}\right]} \quad (A17)$$

714 where z_{0a} is the aeolian roughness length which the surface roughness of overlaying nonerodable
 715 elements and was taken as the minimum of monthly mean gridded aeolian roughness length
 716 (Prigent et al., 2005); $z_{0s} = \frac{D_p}{15}$ is the smooth roughness length which quantifies the roughness of a



717 bed of fine soil particles in the absence of roughness elements (Pierre et al., 2014b); $b_1 = 0.7$, $b_2 =$
 718 0.8 , and $X = 10$ m are empirical constants (Leung et al., 2023). $f_{eff,v}$ is the drag partitioning effects
 719 due to vegetation (Pierre et al., 2014a):

$$720 \quad f_{eff,v} = \frac{K + f_0 c}{K + c} \quad (A18)$$

721 where $f_0 = 0.32$ and $c = 4.8$ are empirical constants (Okin, 2008); K is calculated by $\frac{\pi}{2} (\frac{1}{LAI/LAI_{thr}} -$
 722 $1)$ (Leung et al., 2023; Okin, 2008).

723 The wet fluid threshold velocity u_{*ft} is calculated using Equation (A4), except the dry fluid threshold
 724 velocity u_{*ft0} is calculated by (Shao and Lu, 2000):

$$725 \quad u_{*ft0} = \sqrt{A(\rho_p g D_p + \gamma / D_p) / \rho_a} \quad (A19)$$

726 where $A = 0.0123$ and $\gamma = 1.65 \times 10^{-4} \text{ kg s}^{-2}$ are empirical constants (Darmenova et al., 2009;
 727 Leung et al., 2023); $D_p = 127 \pm 47 \text{ }\mu\text{m}$ is the median diameter of soil particle as evaluated from
 728 various field measurements in Leung et al. (2023).

729 Once the saltation is initialized, the threshold velocity required to maintain the saltation
 730 diminishes, which is defined as the dynamic or impact threshold friction velocity u_{*it} in m s^{-1}
 731 (Martin and Kok, 2018):

$$732 \quad u_{*it} = B_{it} u_{*ft0} \quad (A20)$$

733 where $B_{it} = 0.82$. A prior study suggested that the impact threshold primarily governed the
 734 saltation flux (Martin and Kok, 2018) and thus u_{*it} is adopted as the governing threshold in Equation
 735 (14).

736 The standardized wet fluid threshold friction velocity u_{*st} was proposed and argued as a central
 737 factor to characterize soil aridity by a prior study (Kok et al., 2014):

$$738 \quad u_{*st} = u_{*ft} \sqrt{\rho_a / \rho_{a0}} \quad (A21)$$

739 where $\rho_{a0} = 1.225 \text{ kg m}^{-3}$ is the standard surface air density.



740 The fragmentation exponent of κ quantifies the sensitivity of F_d to u_{*s} and is capped at 3 to prevent
 741 excessive sensitivity of the model to wind speeds according to (Kok et al., 2014; Leung et al., 2024):

$$742 \quad \kappa = C_\kappa \frac{(u_{*st} - u_{*st0})}{u_{*st0}} \quad (A22)$$

743 where $C_\kappa = 2.7 \pm 1.0$ and $u_{*st0} = 0.16 \text{ m s}^{-1}$ are constants.

744 The time-varying soil erodibility coefficient is a function of u_{*st} only (Kok et al., 2014):

$$745 \quad C_d = C_{d0} \exp\left(-C_e \frac{u_{*st} - u_{*st0}}{u_{*st0}}\right) \quad (A23)$$

746 where $C_{d0} = (4.4 \pm 0.5) \times 10^{-5}$ and $C_e = 2.0 \pm 0.3$ are empirical constants.

747



748 Table A1. The mean, median, and standard deviation of surface PM_{2.5} dust measured from 26
 749 SPARTAN sites with at least 10 samples in 5 years from 2019 to 2023 globally. Sites are sorted by
 750 the mean surface PM_{2.5} dust concentrations.

Site	Latitude (°N)	Longitude (°E)	# of samples	Mean ($\mu\text{g m}^{-3}$)	Median ($\mu\text{g m}^{-3}$)	Standard deviation ($\mu\text{g m}^{-3}$)
Abu Dhabi	24.4	54.6	136	14.8	14.1	7.4
Ilorin	8.5	4.7	58	12.2	7.1	17.1
Kanpur	26.5	80.2	18	9.3	6.2	8.2
Dhaka	23.7	90.4	53	7.7	7.4	4.1
Addis Ababa	9.0	38.8	113	5.4	5.0	1.7
Beijing	40.0	116.3	169	4.6	3.9	2.3
Rehovot	31.9	34.8	183	4.4	3.2	4.4
Hanoi	21.0	105.8	11	3.8	3.6	0.6
Haifa	32.8	35.0	141	3.6	2.5	3.7
Seoul	37.6	126.9	87	2.9	2.3	1.6
Fajardo	18.4	-65.6	55	2.6	1.8	2.5
Bujumbura	-3.4	29.4	15	2.6	1.9	1.4
Kaohsiung	22.6	120.3	111	2.2	2.2	0.9
Ulsan	35.6	129.2	86	2.2	1.8	1.5
Pretoria	-25.8	28.3	203	2.0	2.0	0.7
Bandung	-6.9	107.6	33	1.9	1.8	0.6
Johannesburg	-26.2	28.0	162	1.5	1.6	0.5
Singapore	1.3	103.8	15	1.5	1.6	0.3
Mexico City	19.3	-99.2	53	1.4	1.3	0.5
Taipei	25.0	121.5	204	1.3	1.0	0.9
Pasadena	34.2	-118.2	220	0.9	0.8	0.3
Lethbridge	49.7	-112.9	15	0.8	0.8	0.4
Melbourne	-37.8	145.0	39	0.8	0.4	1.0
Downsview	43.8	-79.5	22	0.6	0.6	0.2
Sherbrooke	45.4	-71.9	93	0.4	0.3	0.2
Halifax	44.6	-63.6	141	0.3	0.3	0.1

751

752



Table A2. The values of a global tuning factor C_{tune} used for different simulations.

Simulation	C_{tune}
Emis*	
Emis	2.358×10^{-2}
EmisClay	2.569×10^{-3}
EmisClayWet	2.146×10^{-3}
EmisClayWetLAI _{thr}	2.170×10^{-3}
Emis*PSD	2.945×10^{-3}
Emis*PSD7Bins0.5AD	2.892×10^{-3}
Emis*PSD7Bins0.5ADWetDep	2.832×10^{-3}

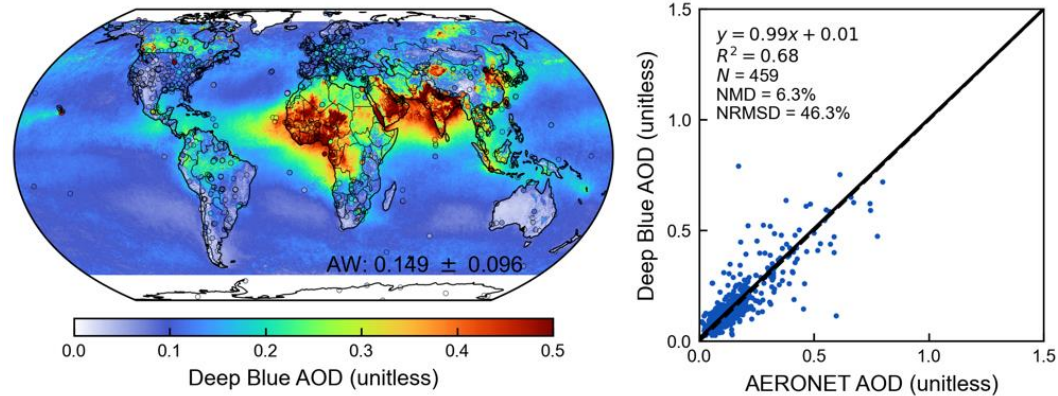
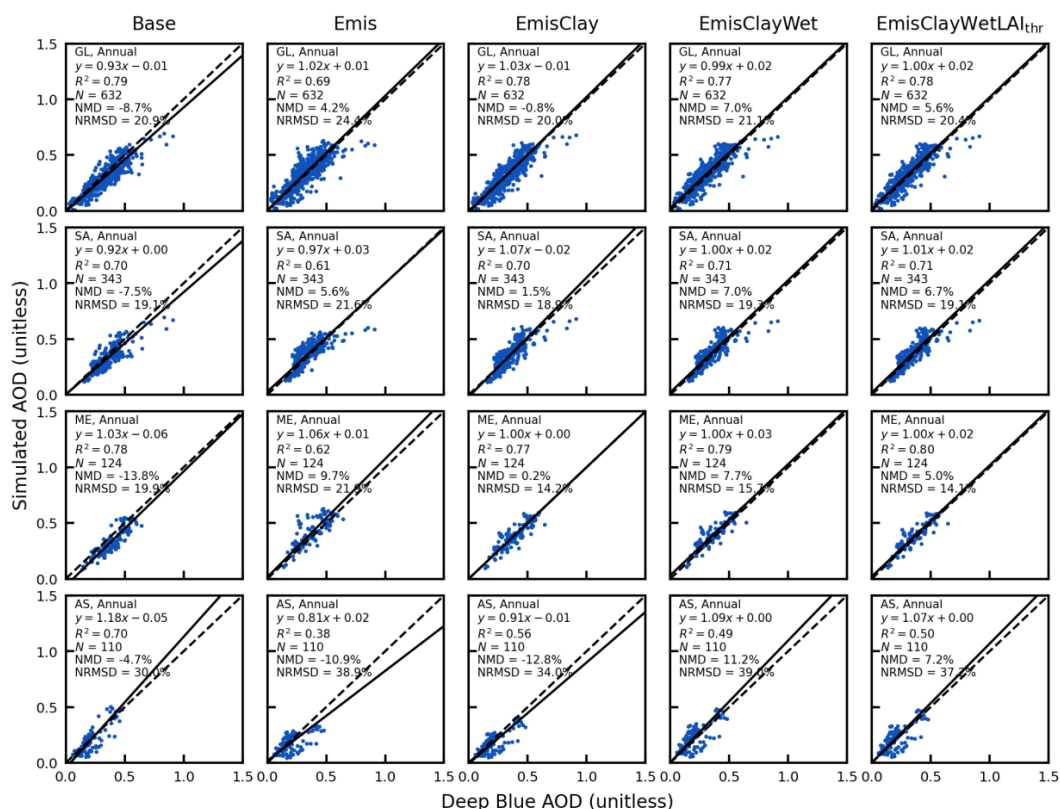


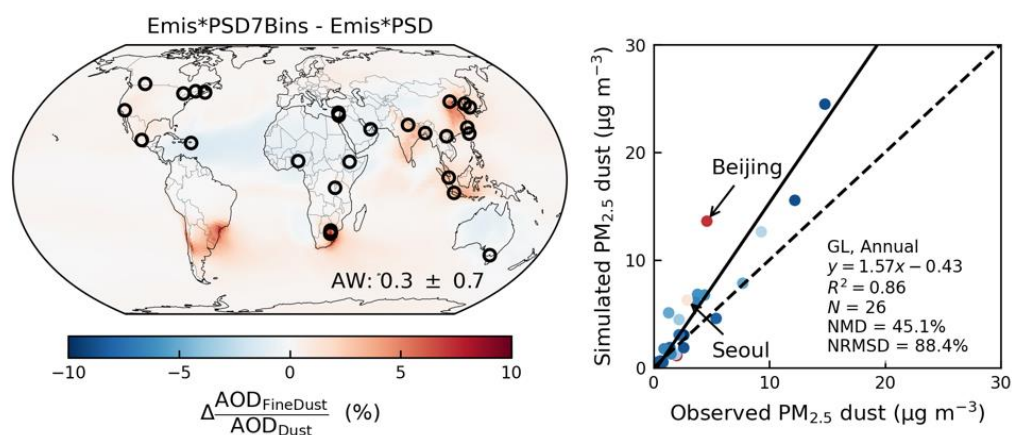
Figure A1. Annual aerosol optical depth (AOD) from the Deep Blue satellite retrieval and comparison against ground-based observations from AERONET in the year of 2018. Filled circles on the map represent ground-based observations from AERONET. Inset values at the bottom right of the map are area-weighted (AW) mean and standard deviation. Regression statistics including the reduced-major-axis linear regression equation, coefficient of variation (R^2), total number of points (N), normalized mean difference (NMD), and normalized root-mean-square difference (NRMSD) are listed at the top left of the scatter plot.



763

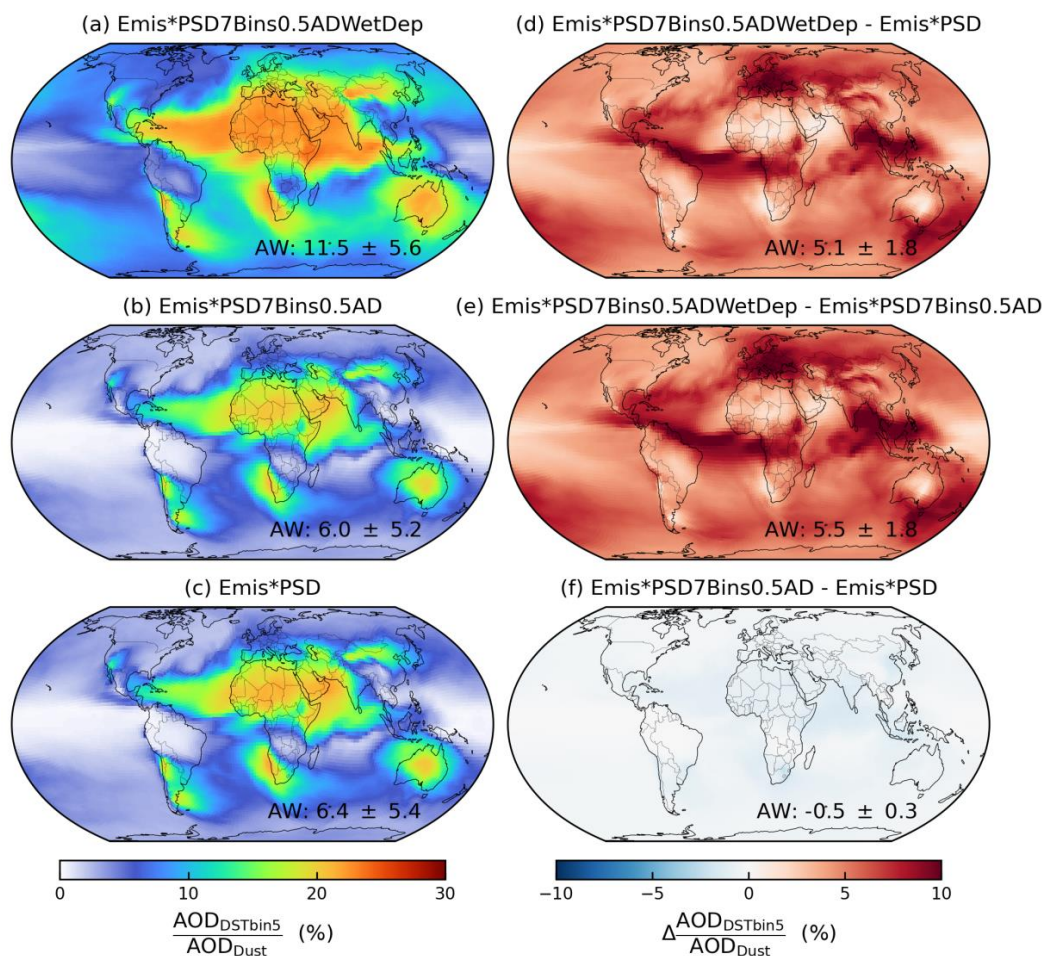
764 Figure A2. Same as Figure 6 but over the same dust source regions for the EmisClayWetLAI_{thr}
 765 scheme for all dust emission scheme comparisons versus Deep Blue AOD.

766



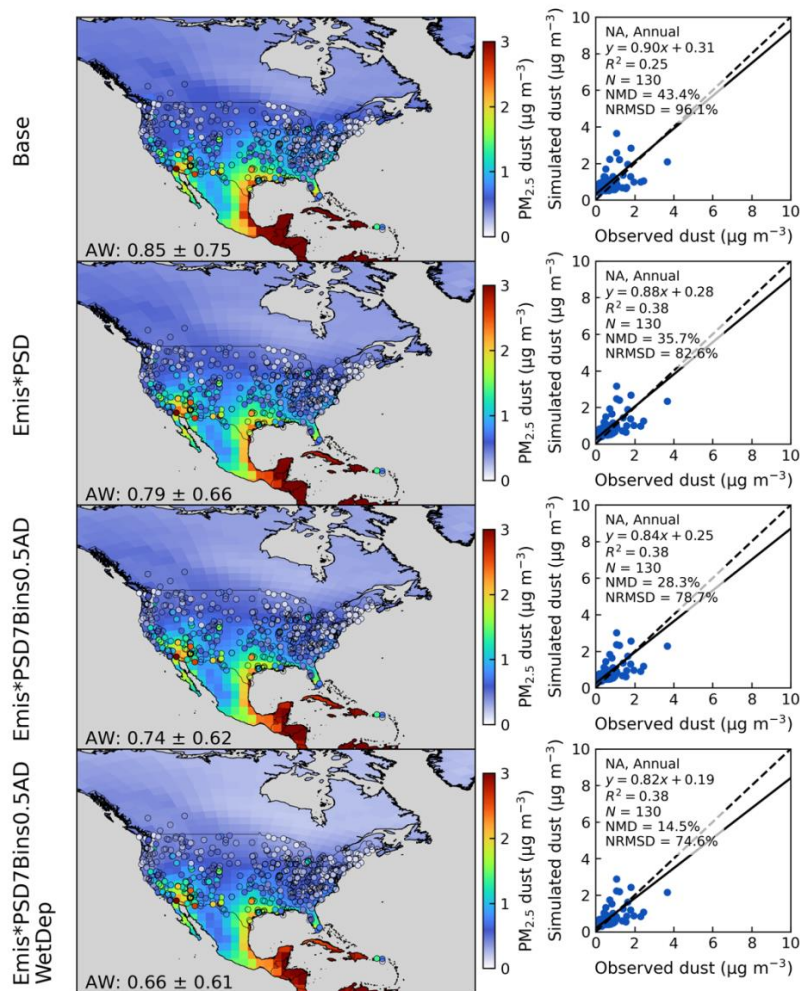
767

768 Figure A3. Differences of the fractional contributions of fine dust with geometric diameter less than
 769 $2 \mu\text{m}$ to total dust column abundance ($AOD_{FineDust}/AOD_{Dust}$) between the Emis*PSD7Bins and
 770 Emis*PSD simulations (left); Comparison between simulated PM_{2.5} dust against SPARTAN
 771 measurements from the Emis*PSD7Bins simulation with color coded by the differences of
 772 $AOD_{FineDust}/AOD_{Dust}$ between the Emis*PSD7Bins and Emis*PSD simulations over SPARTAN
 773 sites. Open circles in the map indicate SPARTAN sites. Inset values at the bottom right of the map
 774 are area-weighted (AW) mean and standard deviation. Regression statistics including the reduced-
 775 major-axis linear regression equation, coefficient of variation (R^2), total number of points (N),
 776 normalized mean difference (NMD), and normalized root-mean-square difference (NRMSD) are
 777 listed at the bottom right of the scatter plot.



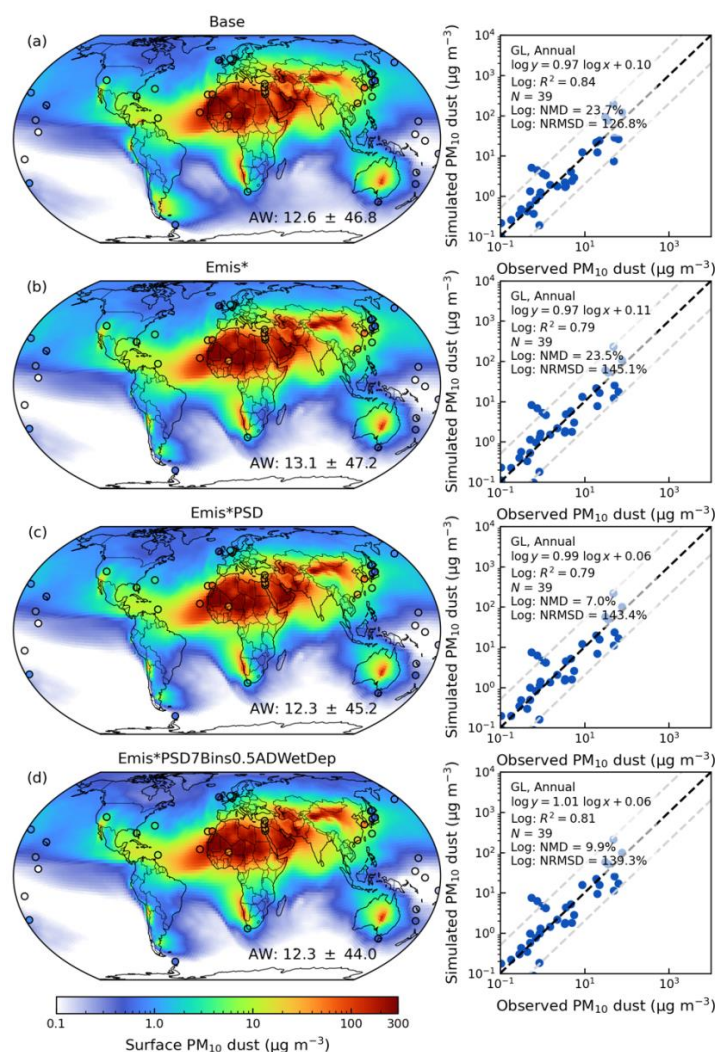
778

779 Figure A4. Fractional contributions of DSTbin5 to total dust column abundance
 780 ($AOD_{DSTbin5}/AOD_{Dust}$) from the a) Emis*PSD7Bins0.5ADWetDep, b) Emis*PSD7Bins0.5AD, c)
 781 Emis*PSD and their absolute differences. Inset values at the bottom right are area-weighted (AW)
 782 mean and standard deviation.



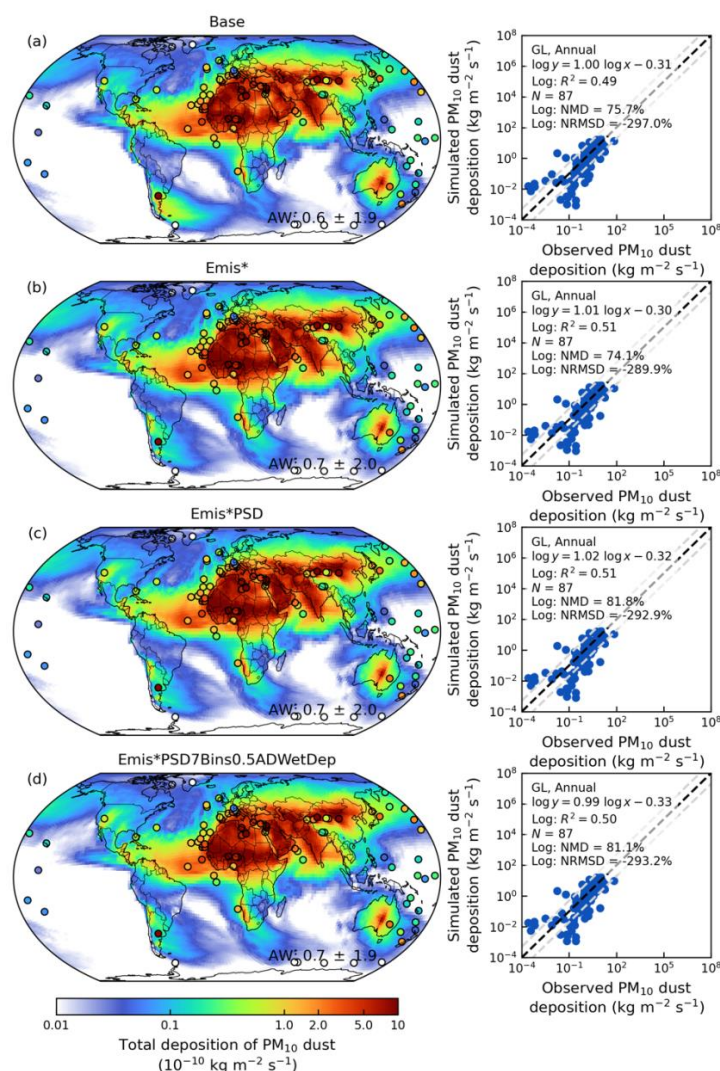
783

784 Figure A5. Comparisons of simulated annual surface $\text{PM}_{2.5}$ dust against ground-based observations
785 in the year of 2018 over North America from the Base (top), Emis*PSD (second),
786 Emis*PSD7Bins0.5AD (third), and Emis*PSD7Bins0.5ADWetDep (bottom) simulations. Filled
787 circles represent ground-based observations of surface $\text{PM}_{2.5}$ dust concentrations. Inset values at
788 the bottom left are area-weighted (AW) mean and standard deviation. Regression statistics
789 including the reduced-major axis linear regression equation, coefficient of variation (R^2), total
790 number of points (N), normalized mean difference (NMD), and normalized root-mean-square
791 difference (NRMSD) are listed at the top left of right panels.



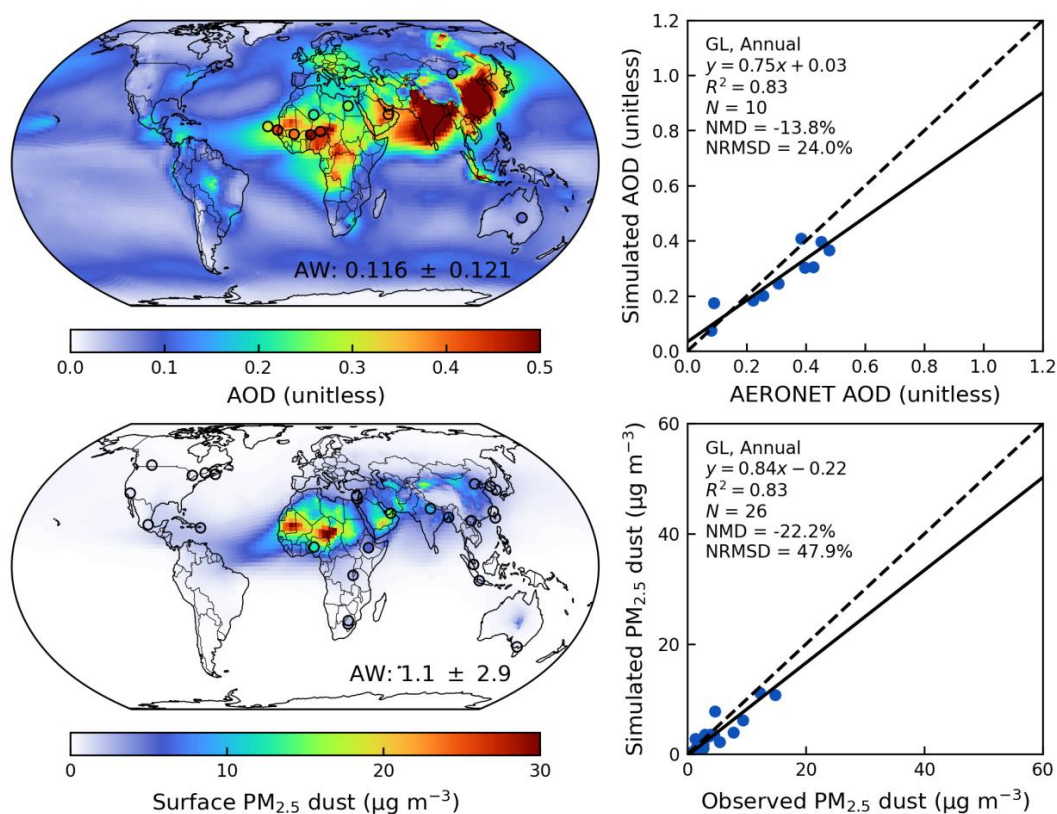
792

793 Figure A6. Annual simulated surface PM₁₀ dust concentrations in the year of 2018 from the
 794 simulations of a) Base, b) Emis*, c) Emis*PSD, and d) Emis*PSD7Bins0.5ADWetDep. Filled circles
 795 represent ground-based observations of surface PM₁₀ dust concentrations. Inset values at the
 796 bottom right are area-weighted (AW) mean and standard deviation. Dash lines in the scatter plots
 797 indicate variations within a factor of 5. Regression statistics including the reduced-major-axis
 798 linear regression equation, coefficient of variation (R^2), total number of points (N), normalized
 799 mean difference (NMD), and normalized root-mean-square difference (NRMSD) are listed at the
 800 top left of right panels.



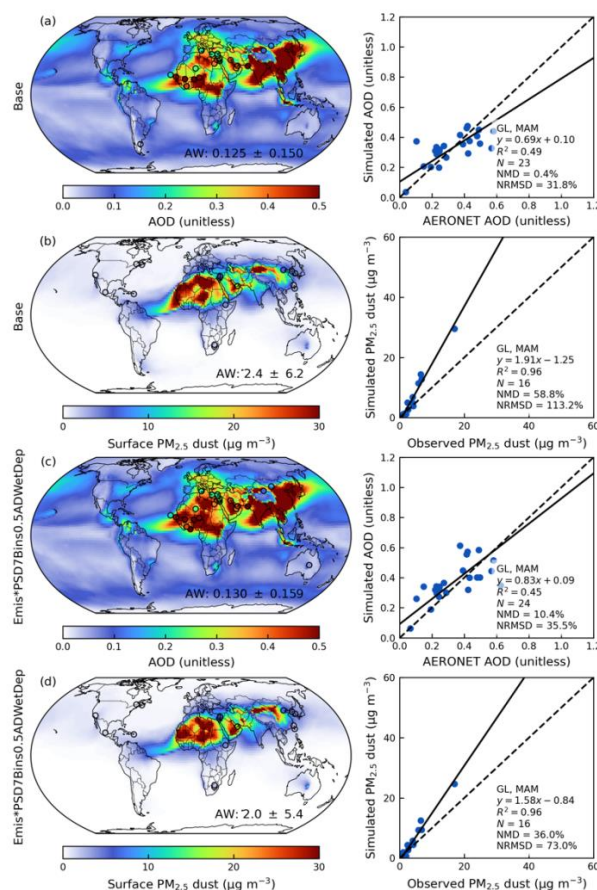
801

802 Figure A7. Annual simulated total deposition of PM₁₀ dust within the troposphere in the year of 2018
 803 from the simulations of a) Base, b) Emis*, c) Emis*PSD, and d) Emis*PSD7Bins0.5ADWetDep.
 804 Filled circles represent ground-based observations of surface PM₁₀ dust deposition. Inset values at
 805 the bottom right are area-weighted (AW) mean and standard deviation. Dash lines in the scatter
 806 plots indicate variations within a factor of 5. Regression statistics including the reduced-major-axis
 807 linear regression equation, coefficient of variation (R^2), total number of points (N), normalized
 808 mean difference (NMD), and normalized root-mean-square difference (NRMSD) are listed at the
 809 top left of right panels.



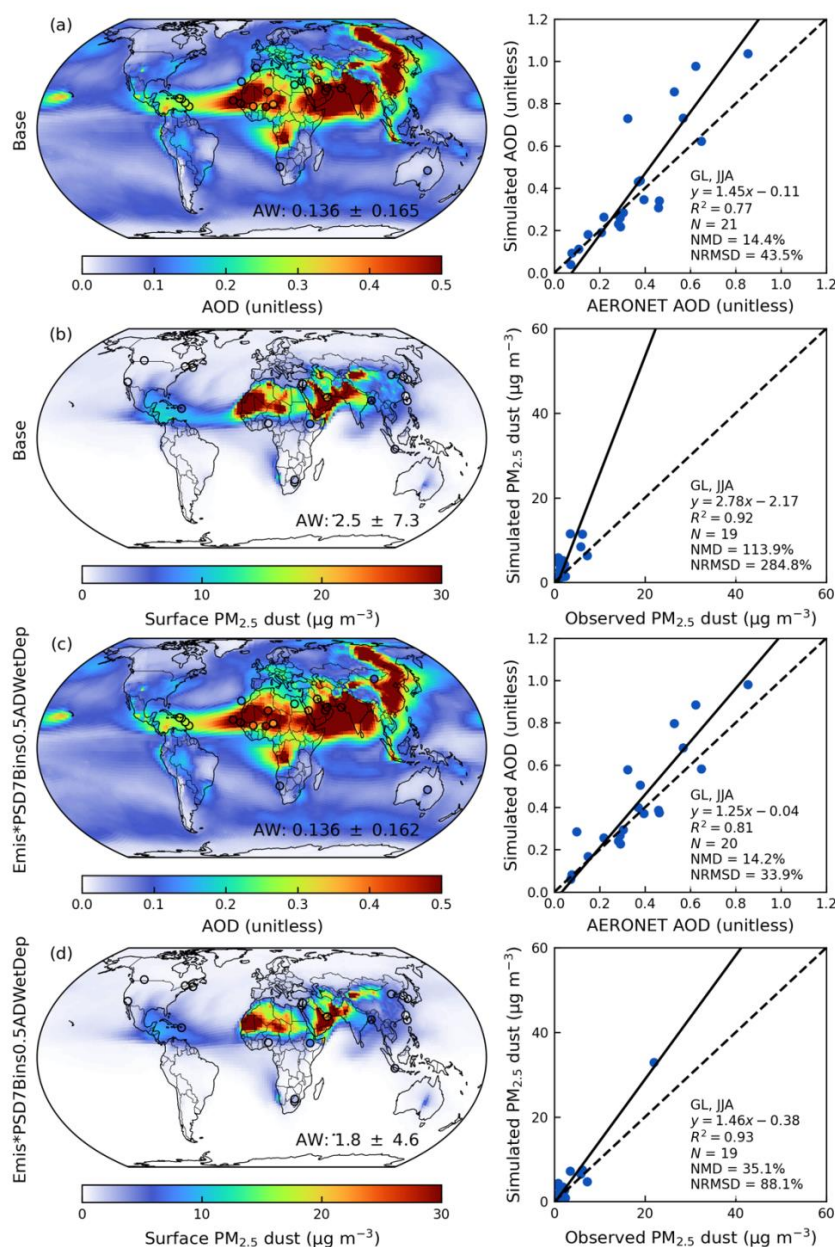
810

811 Figure A8. Annual simulated aerosol optical depth (AOD) and comparison against ground-based
 812 observations from AERONET over dusty regions ($AOD_{Dust}/AOD > 0.5$) (top); Annual simulated
 813 surface $PM_{2.5}$ dust and comparison against ground-based measurements from SPARTAN from the
 814 Emis*PSD7Bins0.5ADWetDep simulation with the dust emissions calculated at C48 resolution in
 815 the year of 2018 (bottom). Filled circles on the maps represent ground-based observations from
 816 SPARTAN and AERONET. Inset values at the bottom right of the maps are area-weighted (AW) mean
 817 and standard deviation. Regression statistics including the reduced-major-axis linear regression
 818 equation, coefficient of variation (R^2), total number of points (N), normalized mean difference
 819 (NMD), and normalized root-mean-square difference (NRMSD) are listed at the top left of the
 820 scatter plots.



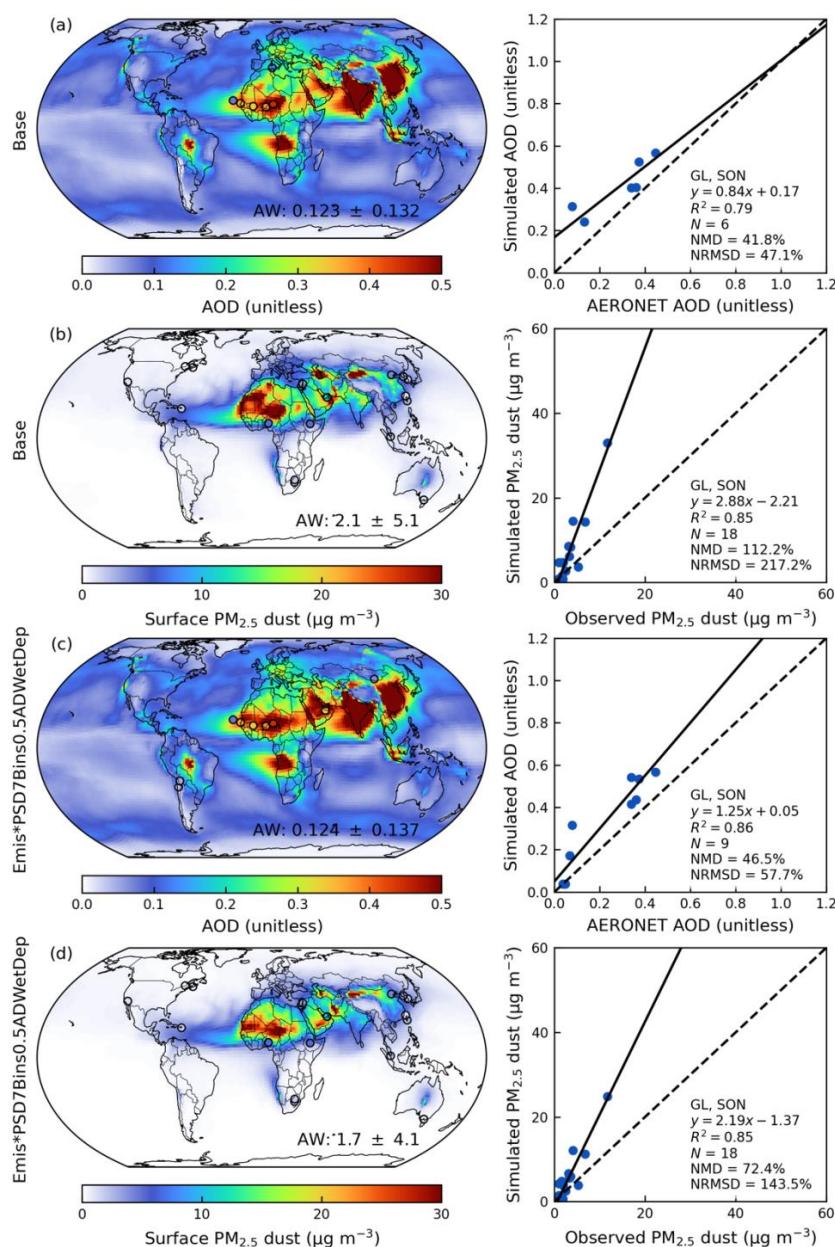
821

822 Figure A9. Simulated seasonal mean (March, April, and May or MAM) aerosol optical depth (AOD; a
 823 and c) and surface PM_{2.5} dust (b and d) from the Base and Emis*PSD7Bins0.5ADWetDep
 824 simulations. Filled circles on the maps represent ground-based observations from SPARTAN and
 825 AERONET. Inset values at the bottom right of the maps are area-weighted (AW) mean and standard
 826 deviation. Comparisons of simulated AOD versus AERONET AOD over dusty sites ($\text{AOD}_{\text{Dust}}/\text{AOD} >$
 827 0.5), and simulated surface PM_{2.5} dust versus SPARTAN observations are shown in the right panels.
 828 Regression statistics including the reduced-major-axis linear regression equation, coefficient of
 829 variation (R^2), total number of points (N), normalized mean difference (NMD), and normalized root-
 830 mean-square difference (NRMSD) are listed at the bottom right of the scatter plots.



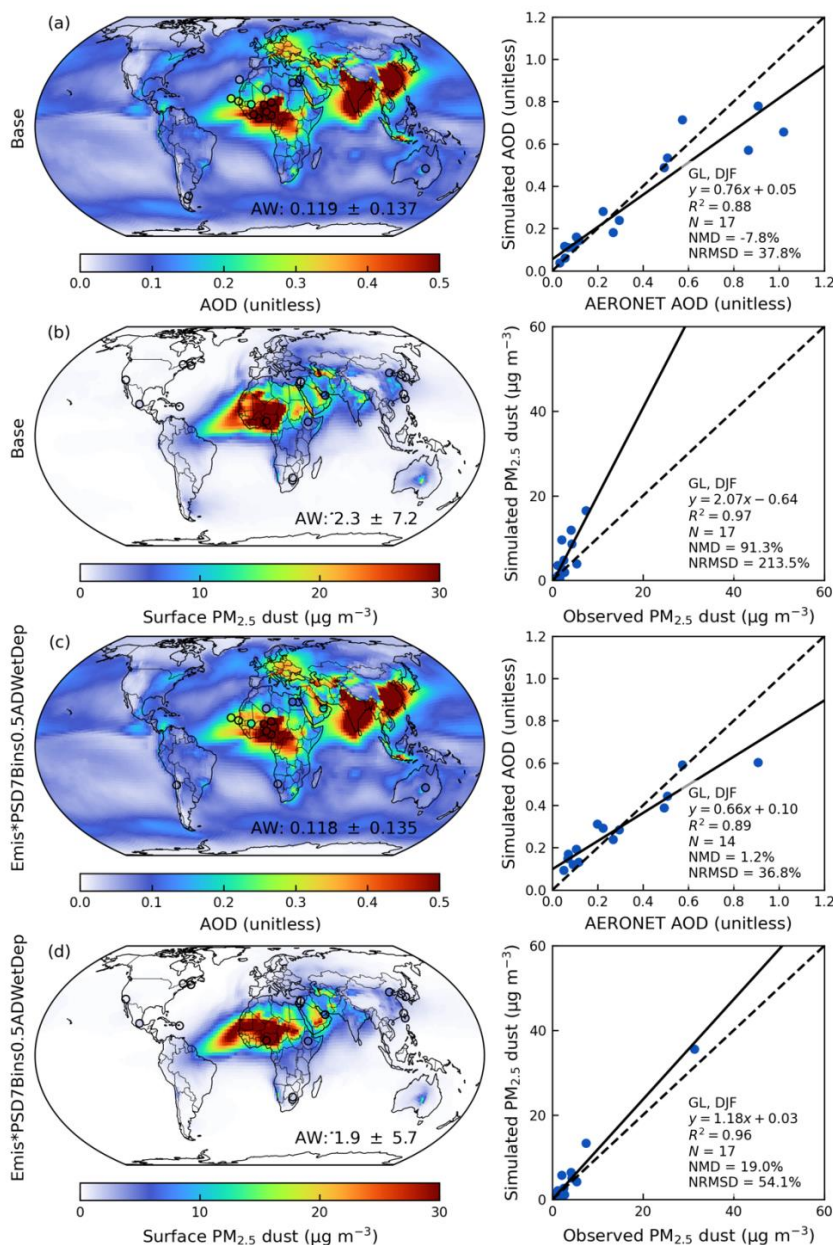
831

832 Figure A10. Same as Figure A9 but for the seasonal mean of June, July, and August (JJA).



833

834 Figure A11. Same as Figure A9 but for the seasonal mean of September, October, and November
 835 (SON).



836

837 Figure A12. Same as Figure A9 but for the seasonal mean of December, January, and February
 838 (DJF).



839 **Code availability.** The standard GEOS-Chem in its high-performance configuration version 14.4.1
840 can be downloaded at <https://doi.org/10.5281/zenodo.12584305> (The International GEOS-Chem
841 User Community, 2024). The model source code, an example run directory, and the calculation
842 scripts for the hourly dust emission fluxes for the revised simulation can be downloaded at
843 <https://doi.org/10.5281/zenodo.14510793> (Zhang, 2024).

844 **Data availability.** The surface $PM_{2.5}$ dust measurements with the attenuation correction from
845 SPARTAN used in this study will be public available in future release at [https://www.spartan-](https://www.spartan-network.org/data)
846 [network.org/data](https://www.spartan-network.org/data) (last access: 4 February 2025). The PM_{10} dust and total deposition of dust are
847 available at <https://doi.org/10.5281/zenodo.6989502> (Li et al., 2022a). The processed
848 meteorological fields from GEOS-FP are available at
849 http://geoschemdata.wustl.edu/ExtData/GEOS_0.25x0.3125/GEOS_FP/ (last access: 4 February
850 2025) with the soil porosity downloaded from the constant land-surface parameter of MERRA2
851 M2C0NXLND collection (<https://disc.gsfc.nasa.gov/datasets?project=MERRA-2>, last access: 4
852 February 2025). The land cover dataset can be downloaded at
853 <https://lpdaac.usgs.gov/products/mcd12c1v061/> (last access: 4 February 2025). The monthly
854 mean leaf area index at 0.5 degree can be downloaded at
855 <http://globalchange.bnu.edu.cn/research/laiv6> (last access: 4 February 2025). The satellite-
856 derived aeolian roughness data are available upon contacting Catherine Prigent. The GSDE soil
857 dataset can be downloaded at <http://globalchange.bnu.edu.cn/research/soilw> (last access: 4
858 February 2025).

859 **Author contribution.** The manuscript was written by DZ and RVM with contributions from all
860 authors. DZ and RVM designed the study with developments of the methodology. DZ conducted
861 simulations and analyzed the results. XL developed the methodology for the mineral dust
862 concentration construction in SPARTAN. AvD compiled the Deep Blue AOD dataset and ground-
863 based observation datasets of surface $PM_{2.5}$ dust over NA and AERONET AOD for evaluation. XL,
864 CRO and EW contributed to SPARTAN measurements. YL contributed to the dry deposition
865 analysis. JM offered valuable discussion for the emission scheme refinements. DML and JFK
866 contributed to the development of a new dust emission scheme. LL constructed the observational
867 data for PM_{10} dust and deposition flux. HZ contributed to the generation of SPARTAN dust data. JRT
868 and YY contributed to the discussion of the evaluation of simulated dust. MB and YR contributed to
869 the establishment and maintenance of SPARTAN monitoring sites. All authors contributed to



870 revising the manuscript.

871 **Competing interests.** The authors declare no competing financial interest.

872 **Acknowledgements.** This work was supported by the National Science Foundation grants
 873 2244984 and 2151093, and the National Aeronautics and Space Administration grant
 874 80NSSC22K0200. The GEOS-FP data used in this study have been provided by the Global Modeling
 875 and Assimilation Office (GMAO) at the NASA Goddard Space Flight Center. We thank the AERONET,
 876 CALIOP, MODIS, and VIIRS teams for the creation and public release of their data products.

877 References

- 878 Bagheri, G. and Bonadonna, C.: On the drag of freely falling non-spherical particles, Powder
 879 Technology, 301, 526–544, <https://doi.org/10.1016/j.powtec.2016.06.015>, 2016.
- 880 Bayon, G., Garzanti, E., Dinis, P., Beaufort, D., Barrat, J.-A., Germain, Y., Trinquier, A., Barbarano,
 881 M., Overare, B., Adeaga, O., and Braquet, N.: Contribution of Saharan dust to chemical weathering
 882 fluxes and associated phosphate release in West Africa, Earth and Planetary Science Letters, 641,
 883 118845, <https://doi.org/10.1016/j.epsl.2024.118845>, 2024.
- 884 Bey, I., Jacob, D. J., Yantosca, R. M., Logan, J. A., Field, B. D., Fiore, A. M., Li, Q., Liu, H. Y., Mickley,
 885 L. J., and Schultz, M. G.: Global modeling of tropospheric chemistry with assimilated meteorology:
 886 Model description and evaluation, Journal of Geophysical Research: Atmospheres, 106, 23073–
 887 23095, <https://doi.org/10.1029/2001JD000807>, 2001.
- 888 Bouwman, A. F., Lee, D. S., Asman, W. A. H., Dentener, F. J., Van Der Hoek, K. W., and Olivier, J. G.
 889 J.: A global high-resolution emission inventory for ammonia, Global Biogeochemical Cycles, 11,
 890 561–587, <https://doi.org/10.1029/97GB02266>, 1997.
- 891 Breider, T. J., Mickley, L. J., Jacob, D. J., Ge, C., Wang, J., Payer Sulprizio, M., Croft, B., Ridley, D. A.,
 892 McConnell, J. R., Sharma, S., Husain, L., Dutkiewicz, V. A., Eleftheriadis, K., Skov, H., and Hopke, P.
 893 K.: Multidecadal trends in aerosol radiative forcing over the Arctic: Contribution of changes in
 894 anthropogenic aerosol to Arctic warming since 1980, Journal of Geophysical Research:
 895 Atmospheres, 122, 3573–3594, <https://doi.org/10.1002/2016JD025321>, 2017.
- 896 Cao, C., De Luccia, F. J., Xiong, X., Wolfe, R., and Weng, F.: Early On-Orbit Performance of the
 897 Visible Infrared Imaging Radiometer Suite Onboard the Suomi National Polar-Orbiting Partnership



- 898 (S-NPP) Satellite, IEEE Transactions on Geoscience and Remote Sensing, 52, 1142–1156,
 899 <https://doi.org/10.1109/TGRS.2013.2247768>, 2014.
- 900 Comola, F., Kok, J. F., Chamecki, M., and Martin, R. L.: The Intermittency of Wind-Driven Sand
 901 Transport, Geophysical Research Letters, 46, 13430–13440,
 902 <https://doi.org/10.1029/2019GL085739>, 2019.
- 903 Croft, B., Wentworth, G. R., Martin, R. V., Leaitch, W. R., Murphy, J. G., Murphy, B. N., Kodros, J. K.,
 904 Abbatt, J. P. D., and Pierce, J. R.: Contribution of Arctic seabird-colony ammonia to atmospheric
 905 particles and cloud-albedo radiative effect, Nature Communications, 7, 13444,
 906 <https://doi.org/10.1038/ncomms13444>, 2016.
- 907 Darmenova, K., Sokolik, I. N., Shao, Y., Marticorena, B., and Bergametti, G.: Development of a
 908 physically based dust emission module within the Weather Research and Forecasting (WRF)
 909 model: Assessment of dust emission parameterizations and input parameters for source regions in
 910 Central and East Asia, Journal of Geophysical Research: Atmospheres, 114, D14201,
 911 <https://doi.org/10.1029/2008JD011236>, 2009.
- 912 Eastham, S. D., Long, M. S., Keller, C. A., Lundgren, E., Yantosca, R. M., Zhuang, J. W., Li, C., Lee, C.
 913 J., Yannetti, M., Auer, B. M., Clune, T. L., Kouatchou, J., Putman, W. M., Thompson, M. A., Trayanov,
 914 A. L., Molod, A. M., Martin, R. V., and Jacob, D. J.: GEOS-Chem High Performance (GCHP v11-02c):
 915 a next-generation implementation of the GEOS-Chem chemical transport model for massively
 916 parallel applications, Geoscientific Model Development, 11, 2941–2953,
 917 <https://doi.org/10.5194/gmd-11-2941-2018>, 2018.
- 918 Emerson, E. W., Hodshire, A. L., DeBolt, H. M., Bilsback, K. R., Pierce, J. R., McMeeking, G. R., and
 919 Farmer, D. K.: Revisiting particle dry deposition and its role in radiative effect estimates,
 920 Proceedings of the National Academy of Sciences, 117, 26076–26082,
 921 <https://doi.org/10.1073/pnas.2014761117>, 2020.
- 922 Fairlie, T. D., Jacob, D. J., and Park, R. J.: The impact of transpacific transport of mineral dust in the
 923 United States, Atmospheric Environment, 41, 1251–1266,
 924 <https://doi.org/10.1016/j.atmosenv.2006.09.048>, 2007.
- 925 Fécan, F., Marticorena, B., and Bergametti, G.: Parametrization of the increase of the aeolian
 926 erosion threshold wind friction velocity due to soil moisture for arid and semi-arid areas, Annales



- 927 Geophysicae, 17, 149–157, <https://doi.org/10.1007/s00585-999-0149-7>, 1999.
- 928 Feng, L., Smith, S. J., Braun, C., Crippa, M., Gidden, M. J., Hoesly, R., Klimont, Z., van Marle, M., van
 929 den Berg, M., and van der Werf, G. R.: The generation of gridded emissions data for CMIP6,
 930 Geoscientific Model Development, 13, 461–482, <https://doi.org/10.5194/gmd-13-461-2020>, 2020.
- 931 Fisher, J. A., Jacob, D. J., Wang, Q., Bahreini, R., Carouge, C. C., Cubison, M. J., Dibb, J. E., Diehl, T.,
 932 Jimenez, J. L., Lebensperger, E. M., Lu, Z., Meinders, M. B. J., Pye, H. O. T., Quinn, P. K., Sharma, S.,
 933 Streets, D. G., Donkelaar, A. van, and Yantosca, R. M.: Sources, distribution, and acidity of sulfate–
 934 ammonium aerosol in the Arctic in winter–spring, Atmospheric Environment, 45, 7301–7318,
 935 <https://doi.org/10.1016/j.atmosenv.2011.08.030>, 2011.
- 936 Giglio, L., Randerson, J. T., and van der Werf, G. R.: Analysis of daily, monthly, and annual burned
 937 area using the fourth-generation global fire emissions database (GFED4), Journal of Geophysical
 938 Research: Biogeosciences, 118, 317–328, <https://doi.org/10.1002/jgrg.20042>, 2013.
- 939 Giles, D. M., Sinyuk, A., Sorokin, M. G., Schafer, J. S., Smirnov, A., Slutsker, I., Eck, T. F., Holben, B.
 940 N., Lewis, J. R., Campbell, J. R., Welton, E. J., Korkin, S. V., and Lyapustin, A. I.: Advancements in
 941 the Aerosol Robotic Network (AERONET) Version 3 database – automated near-real-time quality
 942 control algorithm with improved cloud screening for Sun photometer aerosol optical depth (AOD)
 943 measurements, Atmospheric Measurement Techniques, 12, 169–209,
 944 <https://doi.org/10.5194/amt-12-169-2019>, 2019.
- 945 Ginoux, P., Chin, M., Tegen, I., Prospero, J. M., Holben, B., Dubovik, O., and Lin, S.-J.: Sources and
 946 distributions of dust aerosols simulated with the GOCART model, Journal of Geophysical
 947 Research: Atmospheres, 106, 20255–20273, <https://doi.org/10.1029/2000JD000053>, 2001.
- 948 González-Flórez, C., Klose, M., Alastuey, A., Dupont, S., Escibano, J., Etyemezian, V., Gonzalez-
 949 Romero, A., Huang, Y., Kandler, K., Nikolich, G., Panta, A., Querol, X., Reche, C., Yus-Díez, J., and
 950 Pérez García-Pando, C.: Insights into the size-resolved dust emission from field measurements in
 951 the Moroccan Sahara, Atmospheric Chemistry and Physics, 23, 7177–7212,
 952 <https://doi.org/10.5194/acp-23-7177-2023>, 2023.
- 953 Harris, L., Zhou, L., Lin, S.-J., Chen, J.-H., Chen, X., Gao, K., Morin, M., Rees, S., Sun, Y., Tong, M.,
 954 Xiang, B., Bender, M., Benson, R., Cheng, K.-Y., Clark, S., Elbert, O. D., Hazelton, A., Huff, J. J.,
 955 Kaltenbaugh, A., Liang, Z., Marchok, T., Shin, H. H., and Stern, W.: GFDL SHiELD: A Unified System



- 956 for Weather-to-Seasonal Prediction, *Journal of Advances in Modeling Earth Systems*, 12,
 957 e2020MS002223, <https://doi.org/10.1029/2020MS002223>, 2020.
- 958 Hsu, N. C., Lee, J., Sayer, A. M., Kim, W., Bettenhausen, C., and Tsay, S.-C.: VIIRS Deep Blue
 959 Aerosol Products Over Land: Extending the EOS Long-Term Aerosol Data Records, *Journal of*
 960 *Geophysical Research: Atmospheres*, 124, 4026–4053, <https://doi.org/10.1029/2018JD029688>,
 961 2019.
- 962 Hu, L., Keller, C. A., Long, M. S., Sherwen, T., Auer, B., Da Silva, A., Nielsen, J. E., Pawson, S.,
 963 Thompson, M. A., Trayanov, A. L., Travis, K. R., Grange, S. K., Evans, M. J., and Jacob, D. J.: Global
 964 simulation of tropospheric chemistry at 12.5 km resolution: performance and evaluation of the
 965 GEOS-Chem chemical module (v10-1) within the NASA GEOS Earth system model (GEOS-5 ESM),
 966 *Geoscientific Model Development*, 11, 4603–4620, <https://doi.org/10.5194/gmd-11-4603-2018>,
 967 2018.
- 968 Huang, Y., Kok, J. F., Kandler, K., Lindqvist, H., Nousiainen, T., Sakai, T., Adebisi, A., and Jokinen,
 969 O.: Climate Models and Remote Sensing Retrievals Neglect Substantial Desert Dust Asphericity,
 970 *Geophysical Research Letters*, 47, e2019GL086592, <https://doi.org/10.1029/2019GL086592>, 2020.
- 971 Huang, Y., Adebisi, A. A., Formenti, P., and Kok, J. F.: Linking the Different Diameter Types of
 972 Aspherical Desert Dust Indicates That Models Underestimate Coarse Dust Emission, *Geophysical*
 973 *Research Letters*, 48, e2020GL092054, <https://doi.org/10.1029/2020GL092054>, 2021.
- 974 Huneeus, N., Schulz, M., Balkanski, Y., Griesfeller, J., Prospero, J., Kinne, S., Bauer, S., Boucher, O.,
 975 Chin, M., Dentener, F., Diehl, T., Easter, R., Fillmore, D., Ghan, S., Ginoux, P., Grini, A., Horowitz, L.,
 976 Koch, D., Krol, M. C., Landing, W., Liu, X., Mahowald, N., Miller, R., Morcrette, J.-J., Myhre, G.,
 977 Penner, J., Perlwitz, J., Stier, P., Takemura, T., and Zender, C. S.: Global dust model
 978 intercomparison in AeroCom phase I, *Atmospheric Chemistry and Physics*, 11, 7781–7816,
 979 <https://doi.org/10.5194/acp-11-7781-2011>, 2011.
- 980 Iversen, J. D. and White, B. R.: Saltation threshold on Earth, Mars and Venus, *Sedimentology*, 29,
 981 111–119, <https://doi.org/10.1111/j.1365-3091.1982.tb01713.x>, 1982.
- 982 Jaeglé, L., Quinn, P. K., Bates, T. S., Alexander, B., and Lin, J.-T.: Global distribution of sea salt
 983 aerosols: new constraints from in situ and remote sensing observations, *Atmospheric Chemistry*
 984 *and Physics*, 11, 3137–3157, <https://doi.org/10.5194/acp-11-3137-2011>, 2011.



- 985 Jickells, T. D., An, Z. S., Andersen, K. K., Baker, A. R., Bergametti, G., Brooks, N., Cao, J. J., Boyd, P.
986 W., Duce, R. A., Hunter, K. A., Kawahata, H., Kubilay, N., laRoche, J., Liss, P. S., Mahowald, N.,
987 Prospero, J. M., Ridgwell, A. J., Tegen, I., and Torres, R.: Global Iron Connections Between Desert
988 Dust, Ocean Biogeochemistry, and Climate, *Science*, 308, 67–71,
989 <https://doi.org/10.1126/science.1105959>, 2005.
- 990 Jones, A. C., Hill, A., Hemmings, J., Lemaitre, P., Quérel, A., Ryder, C. L., and Woodward, S.: Below-
991 cloud scavenging of aerosol by rain: a review of numerical modelling approaches and sensitivity
992 simulations with mineral dust in the Met Office’s Unified Model, *Atmospheric Chemistry and*
993 *Physics*, 22, 11381–11407, <https://doi.org/10.5194/acp-22-11381-2022>, 2022.
- 994 Kenny, L. C., Gussman, R., and Meyer, M.: Development of a Sharp-Cut Cyclone for Ambient
995 Aerosol Monitoring Applications, *Aerosol Science and Technology*, 32, 338–358,
996 <https://doi.org/10.1080/027868200303669>, 2000.
- 997 Kok, J. F.: A scaling theory for the size distribution of emitted dust aerosols suggests climate
998 models underestimate the size of the global dust cycle, *Proceedings of the National Academy of*
999 *Sciences*, 108, 1016–1021, <https://doi.org/10.1073/pnas.1014798108>, 2011.
- 1000 Kok, J. F., Mahowald, N. M., Fratini, G., Gillies, J. A., Ishizuka, M., Leys, J. F., Mikami, M., Park, M.-S.,
1001 Park, S.-U., Van Pelt, R. S., and Zobeck, T. M.: An improved dust emission model – Part 1: Model
1002 description and comparison against measurements, *Atmospheric Chemistry and Physics*, 14,
1003 13023–13041, <https://doi.org/10.5194/acp-14-13023-2014>, 2014.
- 1004 Kok, J. F., Ridley, D. A., Zhou, Q., Miller, R. L., Zhao, C., Heald, C. L., Ward, D. S., Albani, S., and
1005 Haustein, K.: Smaller desert dust cooling effect estimated from analysis of dust size and
1006 abundance, *Nature Geoscience*, 10, 274–278, <https://doi.org/10.1038/ngeo2912>, 2017.
- 1007 Kok, J. F., Adebisi, A. A., Albani, S., Balkanski, Y., Checa-Garcia, R., Chin, M., Colarco, P. R.,
1008 Hamilton, D. S., Huang, Y., Ito, A., Klose, M., Leung, D. M., Li, L., Mahowald, N. M., Miller, R. L.,
1009 Obiso, V., Pérez García-Pando, C., Rocha-Lima, A., Wan, J. S., and Whicker, C. A.: Improved
1010 representation of the global dust cycle using observational constraints on dust properties and
1011 abundance, *Atmospheric Chemistry and Physics*, 21, 8127–8167, [https://doi.org/10.5194/acp-21-](https://doi.org/10.5194/acp-21-8127-2021)
1012 8127-2021, 2021.
- 1013 Latimer, R. N. C. and Martin, R. V.: Interpretation of measured aerosol mass scattering efficiency



- 1014 over North America using a chemical transport model, *Atmospheric Chemistry and Physics*, 19,
1015 2635–2653, <https://doi.org/10.5194/acp-19-2635-2019>, 2019.
- 1016 Leung, D. M., Kok, J. F., Li, L., Okin, G. S., Prigent, C., Klose, M., Pérez García-Pando, C., Menut, L.,
1017 Mahowald, N. M., Lawrence, D. M., and Chamecki, M.: A new process-based and scale-aware
1018 desert dust emission scheme for global climate models – Part I: Description and evaluation against
1019 inverse modeling emissions, *Atmospheric Chemistry and Physics*, 23, 6487–6523,
1020 <https://doi.org/10.5194/acp-23-6487-2023>, 2023.
- 1021 Leung, D. M., Kok, J. F., Li, L., Mahowald, N. M., Lawrence, D. M., Tilmes, S., Kluzek, E., Klose, M.,
1022 and Pérez García-Pando, C.: A new process-based and scale-aware desert dust emission scheme
1023 for global climate models – Part II: Evaluation in the Community Earth System Model version 2
1024 (CESM2), *Atmospheric Chemistry and Physics*, 24, 2287–2318, [https://doi.org/10.5194/acp-24-](https://doi.org/10.5194/acp-24-2287-2024)
1025 2287-2024, 2024.
- 1026 Li, L., Mahowald, N. M., Kok, J. F., Liu, X., Wu, M., Leung, D. M., Hamilton, D. S., Emmons, L. K.,
1027 Huang, Y., Sexton, N., Meng, J., and Wan, J.: Data and codes for “Importance of different
1028 parameterization changes for the updated dust cycle modelling in the Community Atmosphere
1029 Model (version 6.1),” <https://doi.org/10.5281/zenodo.6989502>, 2022a.
- 1030 Li, L., Mahowald, N. M., Kok, J. F., Liu, X., Wu, M., Leung, D. M., Hamilton, D. S., Emmons, L. K.,
1031 Huang, Y., Sexton, N., Meng, J., and Wan, J.: Importance of different parameterization changes for
1032 the updated dust cycle modeling in the Community Atmosphere Model (version 6.1), *Geoscientific
1033 Model Development*, 15, 8181–8219, <https://doi.org/10.5194/gmd-15-8181-2022>, 2022b.
- 1034 Liao, H. and Seinfeld, J. H.: Radiative forcing by mineral dust aerosols: Sensitivity to key variables,
1035 *Journal of Geophysical Research: Atmospheres*, 103, 31637–31645,
1036 <https://doi.org/10.1029/1998JD200036>, 1998.
- 1037 Lin, H., Jacob, D. J., Lundgren, E. W., Sulprizio, M. P., Keller, C. A., Fritz, T. M., Eastham, S. D.,
1038 Emmons, L. K., Campbell, P. C., Baker, B., Saylor, R. D., and Montuoro, R.: Harmonized Emissions
1039 Component (HEMCO) 3.0 as a versatile emissions component for atmospheric models: application
1040 in the GEOS-Chem, NASA GEOS, WRF-GC, CESM2, NOAA GEFS-Aerosol, and NOAA UFS models,
1041 *Geosci. Model Dev.*, 14, 5487–5506, <https://doi.org/10.5194/gmd-14-5487-2021>, 2021.
- 1042 Liu, H., Jacob, D. J., Bey, I., and Yantosca, R. M.: Constraints from ²¹⁰Pb and ⁷Be on wet deposition



- 1043 and transport in a global three-dimensional chemical tracer model driven by assimilated
- 1044 meteorological fields, *Journal of Geophysical Research: Atmospheres*, 106, 12109–12128,
- 1045 <https://doi.org/10.1029/2000JD900839>, 2001.
- 1046 Liu, X., Turner, J. R., Hand, J. L., Schichtel, B. A., and Martin, R. V.: A Global-Scale Mineral Dust
- 1047 Equation, *Journal of Geophysical Research: Atmospheres*, 127, e2022JD036937,
- 1048 <https://doi.org/10.1029/2022JD036937>, 2022.
- 1049 Liu, X., Turner, J. R., Oxford, C. R., McNeill, J., Walsh, B., Le Roy, E., Weagle, C. L., Stone, E., Zhu,
- 1050 H., Liu, W., Wei, Z., Hyslop, N. P., Giacomo, J., Dillner, A. M., Salam, A., Hossen, A., Islam, Z.,
- 1051 Abboud, I., Akoshile, C., Amador-Muñoz, O., Anh, N. X., Asfaw, A., Balasubramanian, R., Chang, R.
- 1052 Y.-W., Coburn, C., Dey, S., Diner, D. J., Dong, J., Farrah, T., Gahungu, P., Garland, R. M., Grutter de
- 1053 la Mora, M., Hasheminassab, S., John, J., Kim, J., Kim, J. S., Langerman, K., Lee, P.-C., Lestari, P.,
- 1054 Liu, Y., Mamo, T., Martins, M., Mayol-Bracero, O. L., Naidoo, M., Park, S. S., Schechner, Y.,
- 1055 Schofield, R., Tripathi, S. N., Windwer, E., Wu, M.-T., Zhang, Q., Brauer, M., Rudich, Y., and Martin,
- 1056 R. V.: Elemental Characterization of Ambient Particulate Matter for a Globally Distributed
- 1057 Monitoring Network: Methodology and Implications, *ACS EST Air*, 1, 283–293,
- 1058 <https://doi.org/10.1021/acsestair.3c00069>, 2024.
- 1059 Mahowald, N., Kohfeld, K., Hansson, M., Balkanski, Y., Harrison, S. P., Prentice, I. C., Schulz, M.,
- 1060 and Rodhe, H.: Dust sources and deposition during the last glacial maximum and current climate:
- 1061 A comparison of model results with paleodata from ice cores and marine sediments, *Journal of*
- 1062 *Geophysical Research: Atmospheres*, 104, 15895–15916, <https://doi.org/10.1029/1999JD900084>,
- 1063 1999.
- 1064 Mahowald, N., Albani, S., Kok, J. F., Engelstaeder, S., Scanza, R., Ward, D. S., and Flanner, M. G.:
- 1065 The size distribution of desert dust aerosols and its impact on the Earth system, *Aeolian Research*,
- 1066 15, 53–71, <https://doi.org/10.1016/j.aeolia.2013.09.002>, 2014.
- 1067 Marticorena, B. and Bergametti, G.: Modeling the atmospheric dust cycle: 1. Design of a soil-
- 1068 derived dust emission scheme, *Journal of Geophysical Research: Atmospheres*, 100, 16415–
- 1069 16430, <https://doi.org/10.1029/95JD00690>, 1995.
- 1070 Martin, R. L. and Kok, J. F.: Distinct Thresholds for the Initiation and Cessation of Aeolian Saltation
- 1071 From Field Measurements, *Journal of Geophysical Research: Earth Surface*, 123, 1546–1565,
- 1072 <https://doi.org/10.1029/2017JF004416>, 2018.



- 1073 Martin, R. V., Eastham, S. D., Bindle, L., Lundgren, E. W., Clune, T. L., Keller, C. A., Downs, W.,
 1074 Zhang, D., Lucchesi, R. A., Sulprizio, M. P., Yantosca, R. M., Li, Y., Estrada, L., Putman, W. M., Auer,
 1075 B. M., Trayanov, A. L., Pawson, S., and Jacob, D. J.: Improved advection, resolution, performance,
 1076 and community access in the new generation (version 13) of the high-performance GEOS-Chem
 1077 global atmospheric chemistry model (GCHP), *Geoscientific Model Development*, 15, 8731–8748,
 1078 <https://doi.org/10.5194/gmd-15-8731-2022>, 2022.
- 1079 Meng, J., Martin, R. V., Ginoux, P., Hammer, M., Sulprizio, M. P., Ridley, D. A., and van Donkelaar,
 1080 A.: Grid-independent high-resolution dust emissions (v1.0) for chemical transport models:
 1081 application to GEOS-Chem (12.5.0), *Geoscientific Model Development*, 14, 4249–4260,
 1082 <https://doi.org/10.5194/gmd-14-4249-2021>, 2021.
- 1083 Meng, J., Huang, Y., Leung, D. M., Li, L., Adebisi, A. A., Ryder, C. L., Mahowald, N. M., and Kok, J. F.:
 1084 Improved Parameterization for the Size Distribution of Emitted Dust Aerosols Reduces Model
 1085 Underestimation of Super Coarse Dust, *Geophysical Research Letters*, 49, e2021GL097287,
 1086 <https://doi.org/10.1029/2021GL097287>, 2022.
- 1087 Miller, S. J., Makar, P. A., and Lee, C. J.: HETerogeneous vectorized or Parallel (HETPV1.0): an
 1088 updated inorganic heterogeneous chemistry solver for the metastable-state $\text{NH}_4^+ - \text{Na}^+ - \text{Ca}^{2+} - \text{K}^+ -$
 1089 $\text{Mg}^{2+} - \text{SO}_4^{2-} - \text{NO}_3^- - \text{Cl}^- - \text{H}_2\text{O}$ system based on ISORROPIA II, *Geoscientific Model*
 1090 *Development*, 17, 2197–2219, <https://doi.org/10.5194/gmd-17-2197-2024>, 2024.
- 1091 Murray, L. T., Jacob, D. J., Logan, J. A., Hudman, R. C., and Koshak, W. J.: Optimized regional and
 1092 interannual variability of lightning in a global chemical transport model constrained by LIS/OTD
 1093 satellite data, *Journal of Geophysical Research: Atmospheres*, 117, D20307,
 1094 <https://doi.org/10.1029/2012JD017934>, 2012.
- 1095 Mytilinaios, M., Basart, S., Ciamprone, S., Cuesta, J., Dema, C., Di Tomaso, E., Formenti, P.,
 1096 Gkikas, A., Jorba, O., Kahn, R., Pérez García-Pando, C., Trippetta, S., and Mona, L.: Comparison of
 1097 dust optical depth from multi-sensor products and MONARCH (Multiscale Online Non-hydrostatic
 1098 Atmosphere Chemistry) dust reanalysis over North Africa, the Middle East, and Europe,
 1099 *Atmospheric Chemistry and Physics*, 23, 5487–5516, <https://doi.org/10.5194/acp-23-5487-2023>,
 1100 2023.
- 1101 Okin, G. S.: A new model of wind erosion in the presence of vegetation, *Journal of Geophysical*
 1102 *Research: Earth Surface*, 113, <https://doi.org/10.1029/2007JF000758>, 2008.



- 1103 Pai, S. J., Heald, C. L., Pierce, J. R., Farina, S. C., Marais, E. A., Jimenez, J. L., Campuzano-Jost, P.,
 1104 Nault, B. A., Middlebrook, A. M., Coe, H., Shilling, J. E., Bahreini, R., Dingle, J. H., and Vu, K.: An
 1105 evaluation of global organic aerosol schemes using airborne observations, *Atmospheric Chemistry*
 1106 and Physics, 20, 2637–2665, <https://doi.org/10.5194/acp-20-2637-2020>, 2020.
- 1107 Panofsky, H. A., Tennekes, H., Lenschow, D. H., and Wyngaard, J. C.: The characteristics of
 1108 turbulent velocity components in the surface layer under convective conditions, *Boundary-Layer*
 1109 Meteorology, 11, 355–361, <https://doi.org/10.1007/BF02186086>, 1977.
- 1110 Park, R. J., Jacob, D. J., Field, B. D., Yantosca, R. M., and Chin, M.: Natural and transboundary
 1111 pollution influences on sulfate-nitrate-ammonium aerosols in the United States: Implications for
 1112 policy, *Journal of Geophysical Research: Atmospheres*, 109, D15204,
 1113 <https://doi.org/10.1029/2003jd004473>, 2004.
- 1114 Peters, T. M., Kenny, L. C., Gussman, R. A., and Vanderpool, R. W.: Evaluation of PM_{2.5} Size
 1115 Selectors Used in Speciation Samplers, *Aerosol Science and Technology*, 34, 422–429,
 1116 <https://doi.org/10.1080/02786820119266>, 2001.
- 1117 Petroff, A. and Zhang, L.: Development and validation of a size-resolved particle dry deposition
 1118 scheme for application in aerosol transport models, *Geoscientific Model Development*, 3, 753–
 1119 769, <https://doi.org/10.5194/gmd-3-753-2010>, 2010.
- 1120 Philip, S., Martin, R. V., Snider, G., Weagle, C. L., Donkelaar, A. van, Brauer, M., Henze, D. K.,
 1121 Klimont, Z., Venkataraman, C., Guttikunda, S. K., and Zhang, Q.: Anthropogenic fugitive,
 1122 combustion and industrial dust is a significant, underrepresented fine particulate matter source in
 1123 global atmospheric models, *Environmental Research Letters*, 12, 044018,
 1124 <https://doi.org/10.1088/1748-9326/aa65a4>, 2017.
- 1125 Pierre, C., Bergametti, G., Marticorena, B., Kergoat, L., Mougin, E., and Hiernaux, P.: Comparing
 1126 drag partition schemes over a herbaceous Sahelian rangeland, *Journal of Geophysical Research:*
 1127 *Earth Surface*, 119, 2291–2313, <https://doi.org/10.1002/2014JF003177>, 2014a.
- 1128 Pierre, C., Bergametti, G., Marticorena, B., AbdourhamaneTouré, A., Rajot, J.-L., and Kergoat, L.:
 1129 Modeling wind erosion flux and its seasonality from a cultivated sahelian surface: A case study in
 1130 Niger, *CATENA*, 122, 61–71, <https://doi.org/10.1016/j.catena.2014.06.006>, 2014b.
- 1131 Poggio, L., de Sousa, L. M., Batjes, N. H., Heuvelink, G. B. M., Kempen, B., Ribeiro, E., and Rossiter,



- 1132 D.: SoilGrids 2.0: producing soil information for the globe with quantified spatial uncertainty, SOIL,
 1133 7, 217–240, <https://doi.org/10.5194/soil-7-217-2021>, 2021.
- 1134 Prigent, C., Tegen, I., Aires, F., Marticorena, B., and Zribi, M.: Estimation of the aerodynamic
 1135 roughness length in arid and semi-arid regions over the globe with the ERS scatterometer, Journal
 1136 of Geophysical Research: Atmospheres, 110, <https://doi.org/10.1029/2004JD005370>, 2005.
- 1137 Prospero, J. M.: Long-range transport of mineral dust in the global atmosphere: Impact of African
 1138 dust on the environment of the southeastern United States, Proceedings of the National Academy
 1139 of Sciences, 96, 3396–3403, <https://doi.org/10.1073/pnas.96.7.3396>, 1999.
- 1140 Ridley, D. A., Heald, C. L., and Ford, B.: North African dust export and deposition: A satellite and
 1141 model perspective, Journal of Geophysical Research: Atmospheres, 117, D02202,
 1142 <https://doi.org/10.1029/2011JD016794>, 2012.
- 1143 Ridley, D. A., Heald, C. L., Kok, J. F., and Zhao, C.: An observationally constrained estimate of
 1144 global dust aerosol optical depth, Atmospheric Chemistry and Physics, 16, 15097–15117,
 1145 <https://doi.org/10.5194/acp-16-15097-2016>, 2016.
- 1146 Ryder, C. L., Highwood, E. J., Rosenberg, P. D., Trembath, J., Brooke, J. K., Bart, M., Dean, A.,
 1147 Crosier, J., Dorsey, J., Brindley, H., Banks, J., Marsham, J. H., McQuaid, J. B., Sodemann, H., and
 1148 Washington, R.: Optical properties of Saharan dust aerosol and contribution from the coarse mode
 1149 as measured during the Fennec 2011 aircraft campaign, Atmospheric Chemistry and Physics, 13,
 1150 303–325, <https://doi.org/10.5194/acp-13-303-2013>, 2013.
- 1151 Ryu, Y.-H. and Min, S.-K.: Improving Wet and Dry Deposition of Aerosols in WRF-Chem: Updates to
 1152 Below-Cloud Scavenging and Coarse-Particle Dry Deposition, Journal of Advances in Modeling
 1153 Earth Systems, 14, e2021MS002792, <https://doi.org/10.1029/2021MS002792>, 2022.
- 1154 Shangguan, W., Dai, Y., Duan, Q., Liu, B., and Yuan, H.: A global soil data set for earth system
 1155 modeling, Journal of Advances in Modeling Earth Systems, 6, 249–263,
 1156 <https://doi.org/10.1002/2013MS000293>, 2014.
- 1157 Shao, Y. and Lu, H.: A simple expression for wind erosion threshold friction velocity, Journal of
 1158 Geophysical Research: Atmospheres, 105, 22437–22443, <https://doi.org/10.1029/2000JD900304>,
 1159 2000.



- 1160 Singh, I., Martin, R. V., Bindle, L., Chatterjee, D., Li, C., Oxford, C., Xu, X., and Wang, J.: Effect of
 1161 Dust Morphology on Aerosol Optics in the GEOS-Chem Chemical Transport Model, on UV-Vis Trace
 1162 Gas Retrievals, and on Surface Area Available for Reactive Uptake, *Journal of Advances in Modeling*
 1163 *Earth Systems*, 16, e2023MS003746, <https://doi.org/10.1029/2023MS003746>, 2024.
- 1164 Snider, G., Weagle, C. L., Martin, R. V., van Donkelaar, A., Conrad, K., Cunningham, D., Gordon, C.,
 1165 Zwicker, M., Akoshile, C., Artaxo, P., Anh, N. X., Brook, J., Dong, J., Garland, R. M., Greenwald, R.,
 1166 Griffith, D., He, K., Holben, B. N., Kahn, R., Koren, I., Lagrosas, N., Lestari, P., Ma, Z., Vanderlei
 1167 Martins, J., Quel, E. J., Rudich, Y., Salam, A., Tripathi, S. N., Yu, C., Zhang, Q., Zhang, Y., Brauer, M.,
 1168 Cohen, A., Gibson, M. D., and Liu, Y.: SPARTAN: a global network to evaluate and enhance satellite-
 1169 based estimates of ground-level particulate matter for global health applications, *Atmospheric*
 1170 *Measurement Techniques*, 8, 505–521, <https://doi.org/10.5194/amt-8-505-2015>, 2015.
- 1171 Swap, R., Garstang, M., Greco, S., Talbot, R., and Kallberg, P.: Saharan dust in the Amazon Basin,
 1172 *Tellus B*, 44, 133–149, <https://doi.org/10.1034/j.1600-0889.1992.t01-1-00005.x>, 1992.
- 1173 The International GEOS-Chem User Community: geoschem/GCHP: GCHP 14.4.1,
 1174 <https://doi.org/10.5281/zenodo.12584305>, 2024.
- 1175 Tian, R., Ma, X., and Zhao, J.: A revised mineral dust emission scheme in GEOS-Chem:
 1176 improvements in dust simulations over China, *Atmospheric Chemistry and Physics*, 21, 4319–
 1177 4337, <https://doi.org/10.5194/acp-21-4319-2021>, 2021.
- 1178 Uno, I., Wang, Z., Chiba, M., Chun, Y. S., Gong, S. L., Hara, Y., Jung, E., Lee, S.-S., Liu, M., Mikami,
 1179 M., Music, S., Nickovic, S., Satake, S., Shao, Y., Song, Z., Sugimoto, N., Tanaka, T., and Westphal,
 1180 D. L.: Dust model intercomparison (DMIP) study over Asia: Overview, *Journal of Geophysical*
 1181 *Research: Atmospheres*, 111, <https://doi.org/10.1029/2005JD006575>, 2006.
- 1182 Wang, Q., Jacob, D. J., Fisher, J. A., Mao, J., Leibensperger, E. M., Carouge, C. C., Le Sager, P.,
 1183 Kondo, Y., Jimenez, J. L., Cubison, M. J., and Doherty, S. J.: Sources of carbonaceous aerosols and
 1184 deposited black carbon in the Arctic in winter-spring: implications for radiative forcing,
 1185 *Atmospheric Chemistry and Physics*, 11, 12453–12473, [https://doi.org/10.5194/acp-11-12453-](https://doi.org/10.5194/acp-11-12453-2011)
 1186 2011, 2011.
- 1187 Wang, Q., Jacob, D. J., Spackman, J. R., Perring, A. E., Schwarz, J. P., Moteki, N., Marais, E. A., Ge,
 1188 C., Wang, J., and Barrett, S. R. H.: Global budget and radiative forcing of black carbon aerosol:



- 1189 Constraints from pole-to-pole (HIPPO) observations across the Pacific, *Journal of Geophysical*
- 1190 *Research: Atmospheres*, 119, 195–206, <https://doi.org/10.1002/2013jd020824>, 2014a.
- 1191 Wang, X., Zhang, L., and Moran, M. D.: Development of a new semi-empirical parameterization for
- 1192 below-cloud scavenging of size-resolved aerosol particles by both rain and snow, *Geoscientific*
- 1193 *Model Development*, 7, 799–819, <https://doi.org/10.5194/gmd-7-799-2014>, 2014b.
- 1194 Wang, X., Jacob, D. J., Downs, W., Zhai, S., Zhu, L., Shah, V., Holmes, C. D., Sherwen, T., Alexander,
- 1195 B., Evans, M. J., Eastham, S. D., Neuman, J. A., Veres, P. R., Koenig, T. K., Volkamer, R., Huey, L. G.,
- 1196 Bannan, T. J., Percival, C. J., Lee, B. H., and Thornton, J. A.: Global tropospheric halogen (Cl, Br, I)
- 1197 chemistry and its impact on oxidants, *Atmospheric Chemistry and Physics*, 21, 13973–13996,
- 1198 <https://doi.org/10.5194/acp-21-13973-2021>, 2021.
- 1199 Webb, N. P., Chappell, A., LeGrand, S. L., Ziegler, N. P., and Edwards, B. L.: A note on the use of
- 1200 drag partition in aeolian transport models, *Aeolian Research*, 42, 100560,
- 1201 <https://doi.org/10.1016/j.aeolia.2019.100560>, 2020.
- 1202 Weng, H., Lin, J., Martin, R. V., Millet, D. B., Jaeglé, L., Ridley, D., Keller, C., Li, C., Du, M., and Meng,
- 1203 J.: Global high-resolution emissions of soil NO_x, sea salt aerosols, and biogenic volatile organic
- 1204 compounds, *Scientific Data*, 7, 148, <https://doi.org/10.1038/s41597-020-0488-5>, 2020.
- 1205 Wu, C., Lin, Z., and Liu, X.: The global dust cycle and uncertainty in CMIP5 (Coupled Model
- 1206 Intercomparison Project phase 5) models, *Atmospheric Chemistry and Physics*, 20, 10401–10425,
- 1207 <https://doi.org/10.5194/acp-20-10401-2020>, 2020.
- 1208 Wu, C., Lin, Z., Shao, Y., Liu, X., and Li, Y.: Drivers of recent decline in dust activity over East Asia,
- 1209 *Nature Communications*, 13, 7105, <https://doi.org/10.1038/s41467-022-34823-3>, 2022.
- 1210 Young, S. A., Vaughan, M. A., Garnier, A., Tackett, J. L., Lambeth, J. D., and Powell, K. A.: Extinction
- 1211 and optical depth retrievals for CALIPSO's Version 4 data release, *Atmospheric Measurement*
- 1212 *Techniques*, 11, 5701–5727, <https://doi.org/10.5194/amt-11-5701-2018>, 2018.
- 1213 Yuan, H., Dai, Y., Xiao, Z., Ji, D., and Shangguan, W.: Reprocessing the MODIS Leaf Area Index
- 1214 products for land surface and climate modelling, *Remote Sensing of Environment*, 115, 1171–1187,
- 1215 <https://doi.org/10.1016/j.rse.2011.01.001>, 2011.
- 1216 Zender, C. S., Bian, H., and Newman, D.: Mineral Dust Entrainment and Deposition (DEAD) model:



- 1217 Description and 1990s dust climatology, *Journal of Geophysical Research: Atmospheres*, 108,
 1218 <https://doi.org/10.1029/2002JD002775>, 2003.
- 1219 Zhang, D.: Improving Fine Mineral Dust Representation from the Surface to the Column in GEOS-
 1220 Chem version 14.4.1, <https://doi.org/10.5281/zenodo.14510793>, 2024.
- 1221 Zhang, J. and Shao, Y.: A new parameterization of particle dry deposition over rough surfaces,
 1222 *Atmospheric Chemistry and Physics*, 14, 12429–12440, [https://doi.org/10.5194/acp-14-12429-](https://doi.org/10.5194/acp-14-12429-2014)
 1223 2014, 2014.
- 1224 Zhang, L., Gong, S., Padro, J., and Barrie, L.: A size-segregated particle dry deposition scheme for
 1225 an atmospheric aerosol module, *Atmospheric Environment*, 35, 549–560,
 1226 [https://doi.org/10.1016/S1352-2310\(00\)00326-5](https://doi.org/10.1016/S1352-2310(00)00326-5), 2001.
- 1227 Zhang, L., Kok, J. F., Henze, D. K., Li, Q., and Zhao, C.: Improving simulations of fine dust surface
 1228 concentrations over the western United States by optimizing the particle size distribution,
 1229 *Geophysical Research Letters*, 40, 3270–3275, <https://doi.org/10.1002/grl.50591>, 2013.
- 1230 Zhu, H., Martin, R. V., Croft, B., Zhai, S., Li, C., Bindle, L., Pierce, J. R., Chang, R. Y.-W., Anderson, B.
 1231 E., Ziemba, L. D., Hair, J. W., Ferrare, R. A., Hostetler, C. A., Singh, I., Chatterjee, D., Jimenez, J. L.,
 1232 Campuzano-Jost, P., Nault, B. A., Dibb, J. E., Schwarz, J. S., and Weinheimer, A.: Parameterization
 1233 of size of organic and secondary inorganic aerosol for efficient representation of global aerosol
 1234 optical properties, *Atmospheric Chemistry and Physics*, 23, 5023–5042,
 1235 <https://doi.org/10.5194/acp-23-5023-2023>, 2023.
- 1236